



Single-cell RNA sequencing reveals compromised immune microenvironment in precursor stages of multiple myeloma

Oksana Zavidij^{1,2,3,9}, Nicholas J. Haradhvala^{ID 3,4,5,9}, Tarek H. Mouhieddine^{ID 1,2,3,9}, Romanos Sklavenitis-Pistofidis^{1,2,3}, Songjie Cai^{ID 2,6}, Mairead Reidy^{1,2,3}, Mahshid Rahmat^{ID 1,2,3}, Abdallah Flaifel^{2,7}, Benjamin Ferland⁷, Nang K. Su¹, Michael P. Agius^{ID 1,2,3}, Jihye Park^{1,2,3}, Salomon Manier^{1,2}, Mark Bustoros^{1,2,3}, Daisy Huynh¹, Marzia Capelletti^{ID 1,2,3}, Brianna Berrios¹, Chia-Jen Liu^{ID 1,2}, Meng Xiao He^{3,5}, Esteban Braggio⁸, Rafael Fonseca⁸, Yosef E. Maruvka³, Jennifer L. Guerriero^{1,2}, Melissa Goldman^{2,3}, Eliezer M. Van Allen^{ID 1,2,3}, Steven A. McCarroll^{2,3}, Jamil Azzi^{2,6,10}, Gad Getz^{ID 2,3,4,10} and Irene M. Ghobrial^{ID 1,2,3,10}

Precursor states of multiple myeloma (MM) and its native tumor microenvironment need in-depth molecular characterization to better stratify and treat patients at risk. Using single-cell RNA sequencing of bone marrow cells from precursor stages, monoclonal gammopathy of unknown significance and smoldering MM, to full-blown MM alongside healthy donors, we demonstrate early immune changes during patient progression. We find that natural killer cell abundance is frequently increased in the early stages and associated with altered chemokine receptor expression. As early as smoldering MM, we show loss of granzyme K⁺ memory cytotoxic T cells and show their critical role in MM immunosurveillance in mouse models. Finally, we report major histocompatibility complex class II dysregulation in CD14⁺ monocytes, which results in T-cell suppression in vitro. These results provide a comprehensive map of immune changes at play over the evolution of premalignant MM, which will help develop strategies for immune-based patient stratification.

Bone marrow (BM) plasma cell malignancy MM remains an incurable disease¹. Despite the readily detectable monoclonal gammopathy of unknown significance (MGUS) and smoldering MM (SMM) precursor states^{1–3}, treatment is not administered until patients progress to MM. Since early premalignancy not always leads to progression, treatment cannot be justified solely on this basis. Low- and high-risk SMM exhibit 5-year progression rates of 15 and 70%, respectively, compared to a 20-year rate of 2 and 27% for low- and high-risk MGUS^{4,5}. Therefore, further molecular characterization is required to accurately identify and thwart high-risk premalignant MM.

Genomic studies have shown that MGUS/SMM clones may already harbor chromosomal alterations that define MM (translocations involving IgH or hyperdiploidy^{6,7}) and that progression can be driven by the acquisition of events like MYC translocations, 1q gains and TP53 mutations^{7,8}. However, not all patients with MGUS/SMM with a similar genetic makeup eventually progress to MM, implying that further nongenomic alterations may be required for disease progression^{4,9–11}. Indeed, it is becoming more recognized that tumors represent complex ecosystems¹². Not only can tumor behavior be regulated by the extracellular milieu^{13–15}, but emerging evidence documents that compositional and expression changes

of individual immune and stromal components correlate with disease subtypes and prognostic and therapeutic outcomes in breast, colorectal and other solid cancers^{16–20}.

Prior studies have confirmed that the BM microenvironment in MM exhibits dysregulation in receptor signaling²¹, cytokine expression^{21,22} and numerical alterations in T, natural killer (NK) and dendritic cells^{23–26}. MM cells induce immunosuppression, which comprises expansion of regulatory T (T_{reg}) cells^{27,28}, myeloid-derived suppressor cells (MDSCs)^{29,30}, tumor-associated macrophages^{31,32} and dysfunction of NK cells³³. Alterations to the microenvironment have been linked to reduced antitumor responses, induction of angiogenesis, chemotherapy resistance and progression^{27,31,34,35}.

In this study, we used single-cell transcriptomics to dissect the immune microenvironment in the BM in people with MGUS, SMM and overt MM compared to healthy donors. We observe that the tumor microenvironment exhibits substantial alterations beginning at the MGUS stage, with increased populations of NK cells, T cells and nonclassical monocytes. Among T cells, we observe an early accumulation of regulatory and gamma delta T cells, followed by loss of CD8⁺ memory populations and elevation of IFN signaling at the SMM stage. We demonstrate the critical importance of memory T cells for MM immunosurveillance. In CD14⁺

¹Medical Oncology, Dana-Farber Cancer Institute, Boston, MA, USA. ²Harvard Medical School, Boston, MA, USA. ³Broad Institute of MIT and Harvard, Cambridge, MA, USA. ⁴Massachusetts General Hospital, Boston, MA, USA. ⁵Harvard Biophysics Graduate Program, Harvard University, Boston, MA, USA. ⁶Transplantation Research Center, Renal Division, Brigham and Women's Hospital, Boston, MA, USA. ⁷Specialized Histopathology Core, Brigham and Women's Hospital, Boston, MA, USA. ⁸Department of Medicine, Mayo Clinic Arizona, Scottsdale, AZ, USA. ⁹These authors contributed equally: Oksana Zavidij, Nicholas J. Haradhvala, Tarek H. Mouhieddine. ¹⁰These authors jointly supervised this work: Jamil Azzi, Gad Getz, Irene M. Ghobrial.
✉e-mail: gadget@broadinstitute.org; irene_ghobrial@dfci.harvard.edu

monocytes, we find dysregulated expression of major histocompatibility complex (MHC) type II genes. We show that MM cells lead to loss of antigen presentation, inducing a T-cell suppressive phenotype in monocytes. Together, our results characterize transcriptional and compositional changes occurring in the BM compartment during MM progression. They hint at mechanisms of antitumor immune response and immune evasion. Importantly, the immune patterns we observed are often heterogeneous across patients and thus may prove important biomarkers for risk assessment and therapeutic strategies for the prevention of progression in MM.

Results

To better understand the changes occurring in the tumor microenvironment during MM progression, we performed single-cell RNA sequencing (RNA-seq; 10x Genomics) on BM aspirates from patients at varying stages of progression. We sequenced approximately 19,000 CD45⁺/CD138⁻ cells from the microenvironment (approximately 15,000 from MM stages) from patients with MGUS ($n=5$ patients), low-risk SMM (SMM-low; $n=3$), high-risk SMM (SMM-high; $n=8$) and newly diagnosed MM ($n=7$), as well as nine healthy donors (normal BM (NBM), $n=9$; Supplementary Tables 1 and 2). One patient contributed sequential samples (SMM-low-1 and MM-8). Patients with SMM were stratified by risk of progression into low (SMMI) and high (SMMh) based on the Mayo clinic established criteria^{10,36}.

The CD45⁺CD138⁻ subset was isolated using magnetic bead sorting of the BM samples and further in silico cell filtering based on gene expression (Experimental procedures). By clustering cells based on expression profile, we isolated 21 subpopulations. Using (1) the expression of known marker genes (Extended Data Fig. 1) and (2) finding the top differentially expressed genes for each cluster (Supplementary Table 3), we classified our clusters with ten broad cell types, ranging from hematopoietic progenitor cells and pre-B cells to mature populations engaged in the immune response (Fig. 1a).

Compositional alterations in the microenvironment occur early in MM progression. To investigate the relative contribution of different cell types to the microenvironmental repertoire across different stages of disease, we searched for populations that were enriched on average in the disease microenvironment compared to normal BM. Consistent with previous data^{23–26}, we observed a significant enrichment in NK, T and CD16⁺ cells in the diseased BM, as well as a relative decrease in plasmacytoid dendritic cells, immature neutrophils, CD14⁺ monocytes and other progenitor cells (Fig. 1b,c). Several of these alterations could already be observed as early as the MGUS stage. Interestingly, the degree of this compositional shift was not uniform across patients. While BM samples from healthy donors universally had <2% CD16⁺ macrophages and <10% NK cells, patient samples occupied a spectrum from unaltered compositions to approximately 12% CD16⁺ macrophages and approximately 40% NK cells. These changes were observed independent of disease stage or tumor burden, suggesting they were mediated by the properties of the tumor itself or the immune response of the individual patients (Fig. 1c). In particular, NK-cell fractions correlated with the proportion of nonclassical monocytes and this relationship did not correspond to the cytogenetic characteristics of the tumor, disease stage or tumor burden (Fig. 1d).

NK levels were most elevated in patients with immunoglobulin G-secreting tumors, which given their interaction with immunoglobulin G via the Fc receptor III in normal physiology³⁷, could indicate a reason for their presence or be a factor in their failure to clear the disease (Extended Data Fig. 2a). Furthermore, samples with overall increases in NK cells were accompanied by a shift in their phenotype. Subclustering of NK cells revealed three populations: a CXCR4⁺, a CX3CR1⁺/CCL3⁺ and a less frequent IL7R⁺CD62L⁺ population (markers of the classical immature CD56^{bright} subset³⁸)

(Fig. 1e). Notably, we observed a correlation between the overall fraction of NK cells in a given sample and the representation of the CXCR4⁺ subset (Spearman $\rho=0.60$, 95% bootstrapped confidence interval (0.18,0.86), $n=23$, samples with $\geq 5\%$ NK cells; Fig. 1fg and Extended Data Fig. 2b). Samples with enrichment (greater than the median) for NK cell frequency also had significant enrichment for the CXCR4⁺ subset (Fisher exact test, $P=0.012$, $n=23$), while samples with lower NK-cell frequencies displayed a shift toward the CX3CR1⁺ subset (Extended Data Fig. 2c). The current understanding is that CXCR4 is required for NK homing toward CXCL12-producing cells in the BM and signifies less mature NK cells, while CX3CR1 expression causes migration toward BM sinusoids, leading to egress from the BM³⁹. This suggests chemotactic relocation could be the basis for the observed heterogeneity in NK-cell frequency.

To further validate the compositional changes observed in our sequencing data, we performed simultaneous deep phenotyping of viably frozen BM aspirates of patients with MGUS, SMM and MM ($n=13$) and healthy BM controls ($n=4$) using mass cytometry by time-of-flight (CyTOF). Overall, CyTOF data correlated with the RNA-seq results (Extended Data Fig. 3a–c), with the exception that we observed substantially lower neutrophil output from the 10x Genomics assay compared to the CyTOF data. While in CyTOF neutrophils represented 8–50% of live cells in the BM (Extended Data Fig. 3d), the 10x Genomics cell distribution favored T cells and monocytes. Due to low messenger RNA content in mature neutrophils, they may not be distinguishable as cells in single-cell RNA data from empty droplets with ambient RNA. However, this type of bias decreases neutrophil counts in both healthy-donor and MM samples, and thus should not alter the results for comparisons of a given cell type across samples.

Composition of noncytotoxic T cells shows increased T_{reg} numbers and patient-specific heterogeneity. To delve deeper into the T-cell subtypes and states, we used two complementary approaches. First, we performed additional subclustering at higher resolution using genes variably expressed among T cells, resulting in 12 subclusters (Fig. 2). Then, because activation of continuous gene expression modules may not be captured by discrete clustering, we used a Bayesian variant of nonnegative matrix factorization to extract seven expression signatures (Fig. 3). First, we examined the noncytotoxic subsets marked by high expression of signature T-sig1 (Fig. 3a). T-cell clusters distinguished by T-sig1 included three CCR7-expressing naive CD4 subsets, two populations of helper CD4 cells and a population of T_{reg} cells (Fig. 2a–c). An additional cluster of helper CD4 cells showed upregulated interferon (IFN) type I-activated genes; indeed, in our signature analysis we found a corresponding signature of IFN response that was highly upregulated in five late-stage samples (T-sig2, Fig. 4a, 1 SMM-high and four MM). In addition, as described previously^{27,28}, we saw a significant upregulation of T_{reg} cells in the diseased microenvironment (Fig. 2d,e, $q=0.0005$, d.f.=26.1, Benjamini–Hochberg-corrected t -test of NBM versus disease samples). Interestingly, transcriptional profiles of T_{reg} cells demonstrate high expression of MHC type II proteins, which have been reported to inhibit T-cell proliferation and cytokine production via an early contact-dependent mechanism⁴⁰. Additionally, our patient with sequential samples had CD4⁺ subsets that express corticotropin-releasing hormone, which promotes inflammation⁴¹.

Cytotoxic T-cell populations shift toward effector phenotype during disease progression. Our cytotoxic T cells were broadly separated by two signatures of (T-sig4 and T-sig7; Fig. 3a), most notably corresponding to the expression of either granzymes B (GZMB, GrB) and H (GZMH, GrH; T-sig4) or granzyme K (GZMK, GrK; T-sig7; Fig. 3b), present exclusively in CD8⁺ cells. The GrK-to-GrB

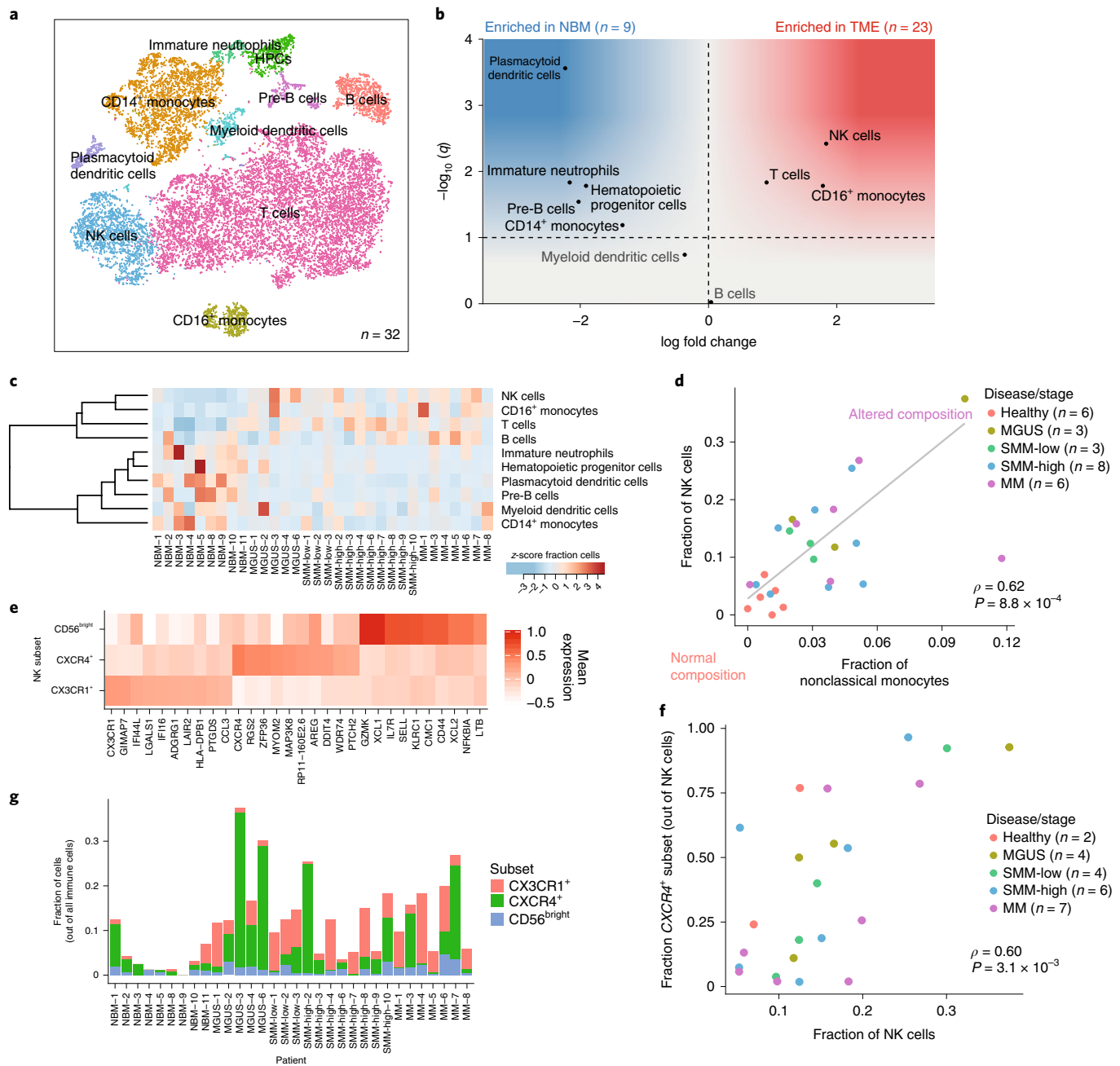


Fig. 1 | The immune landscape in healthy-donor and MM samples. **a**, t-SNE representation of immune cells identified in the CD45⁺ population. **b**, Immune composition changes between normal and cancer samples. For each cell type, the log fold change in mean cell fraction between tumor and normal samples, with $-\log_{10}$ Benjamin-Hochberg-corrected, two-sided Wilcoxon rank-sum P values on the y axis ($n=32$ patient samples) is shown. **c**, Distribution of different cell types in the CD45⁺ fraction for individual patients and healthy donors. Cell type fractions are z-standardized across patients. **d**, Proportion of NK cells correlated with numbers of nonclassical monocyte cell fractions indicating inflammatory environment in patients compared to healthy controls. Only samples with at least 200 total cells are shown. Correlation was assessed by Spearman coefficient on $n=26$ patient samples. **e**, Distribution of NK-cell subsets in the BM microenvironment. The heatmap shows the mean expression of highly represented individual marker genes per cluster. **f**, Scatter plot of the fraction of NK cells in a given patient that are CXCR4⁺ versus the fraction of all immune cells that are NK cells. Only samples with at least 50 NK cells are shown. Correlation was assessed by Spearman coefficient on $n=23$ patient samples. **g**, Proportion of distinct NK-cell subsets per sample. Samples with high NK-cell enrichment are largely composed of the CXCR4⁺ subtype. Only samples with at least 50 NK cells are shown on $n=23$ patient samples.

transition has been associated with the differentiation of cytotoxic T cells from memory to effector state⁴². The T cells marked by the GrB expression signature included clusters of CD8⁺ cytotoxic effector and gamma delta T cells, in addition to a subpopulation of CD4⁺ cytotoxic cells and NK T cells predominantly derived from one patient (Fig. 2d).

Among cells expressing one of two cytotoxic signatures (considered as >100 and >50 activity for signatures T-sig4 and T-sig7 based on their distribution), T-sig7 was more prevalent in healthy individuals and patients with MGUS ($P=0.0013$, d.f.=21.5, $n=30$, t -test on patient mean signature activity across these cytotoxic cells between healthy/MGUS and SMM/MM), whereas

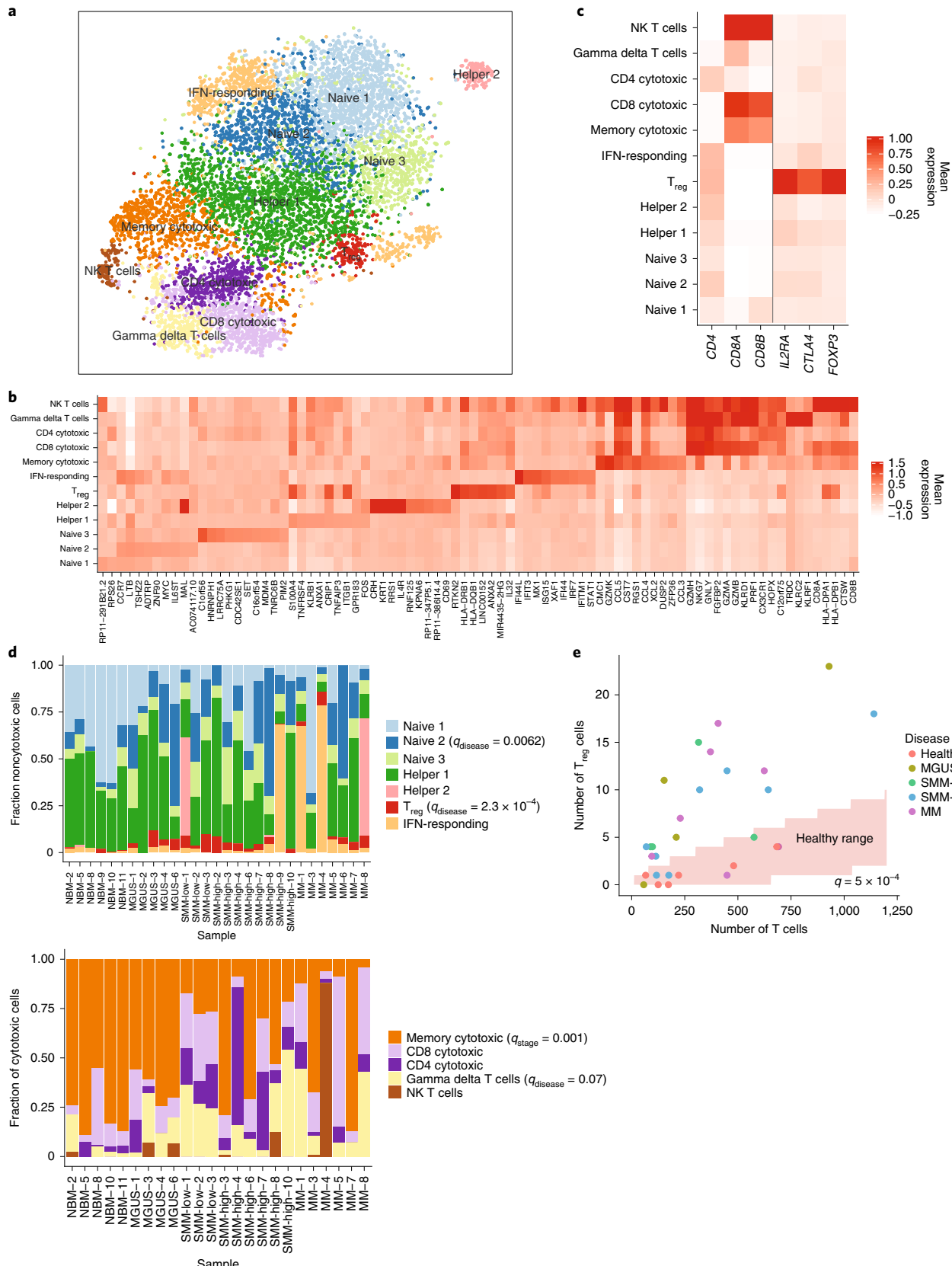


Fig. 2 | Heterogeneous composition of T cells in diseased BM microenvironment. **a**, t-SNE visualization of T-cell clusters localized in the BM. **b**, Mean expression of differentially expressed marker genes per cluster. **c**, Mean expression of individual genes additionally used for cluster definition. **d**, Distribution of noncytotoxic and cytotoxic T-cell populations in individual samples. Only samples with at least 50 cells of the corresponding type are shown. **e**, Significant enrichment of regulatory T cells in the BM of diseased patients ($q = 0.0005$, d.f. = 26.1, Benjamini–Hochberg-corrected, two-tailed t-test on the fraction of T_{reg} cells between NBM and disease samples using $n = 29$ patient samples with at least 50 T cells).

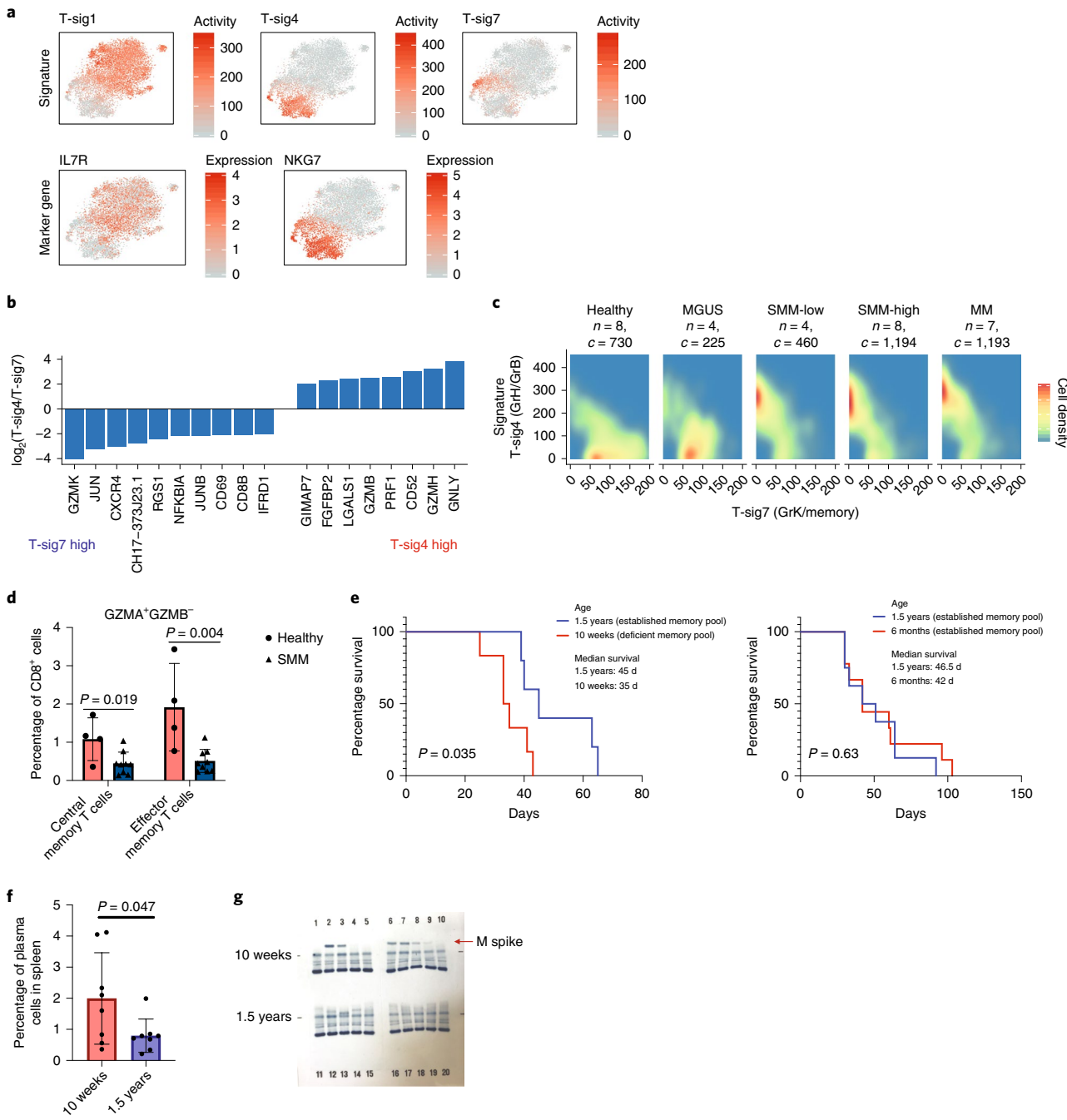


Fig. 3 | Skewed differentiation of cytotoxic T cells in patients with MM at an early disease stage. **a**, t-SNE representation colored by T-cell signature activity and marker genes for broad characteristic signatures. **b**, Log fold change of NMF gene weightings between cytotoxic T-cell signatures T-sig4 and T-sig7. **c**, Distribution of cells expressing GrB/H (T-sig7) and GrK (T-sig4) cytotoxic signatures in healthy donors at different stages of disease. Only T cells expressing one of the two signatures (>100 T-sig4 or >50 T-sig7 activity) are shown. **d**, CyTOF data show decreased numbers of cytotoxic memory cells in the BM of patients SMM compared to healthy donors (with a median value of 1.08 versus 0.45 for central memory T cells; 1.92 versus 0.51 for effector memory T cells in healthy BM and patients with SMM, respectively). CyTOF was performed on CD138⁻ cells from BM aspirates of patients with SMM ($n=9$) and healthy donors ($n=4$) using the GrB-171Yb, GrA-149Sm and Maxpar Human T-Cell Phenotyping Panel Kit, 16 Marker. Cell subsets were defined as suggested by the manufacturer. Significance was tested with a two-tailed t-test; the bars represent the s.d. **e**, Memory cells are critical for immunosurveillance in MM. Significantly shorter survival of 10-week-old KaLwRj mice ($n=6$) after injection with 5TGM1 MM cells, compared to older animals ($n=5$). No difference in survival of myeloma-injected mice was observed in groups with an established memory cell pool (6-month-old KaLwRj mice, $n=9$, versus 1.5-year-old KaLwRj mice, $n=10$). Significance was tested with the log-rank (Mantel-Cox) test. **f**, Early accumulation of CD138⁺ plasma cells in the spleen of 10-week-old BL6 mice ($n=8$) at 3 weeks post Vk^*MYC MM cell injection, compared to older animals ($n=8$), with a median value of 1.99 in younger mice compared to 0.78 in older mice. The significant difference was tested with a two-tailed t-test; the bars represent the s.d. **g**, Faster abundance of monoclonal proteins (M spike) in the blood of 10-week-old BL6 mice ($n=10$) at 3 weeks post Vk^*MYC MM cell injection, compared to 1.5-year-old mice ($n=10$). QuickGel Split-Beta gels separate serum proteins by the classic electrophoresis zones, with monoclonal proteins appearing as a specific band (M spike). The gel has been cut from the outside; no samples/bands were removed. The experiment was repeated twice with the same results. Representative data from one experiment is shown.

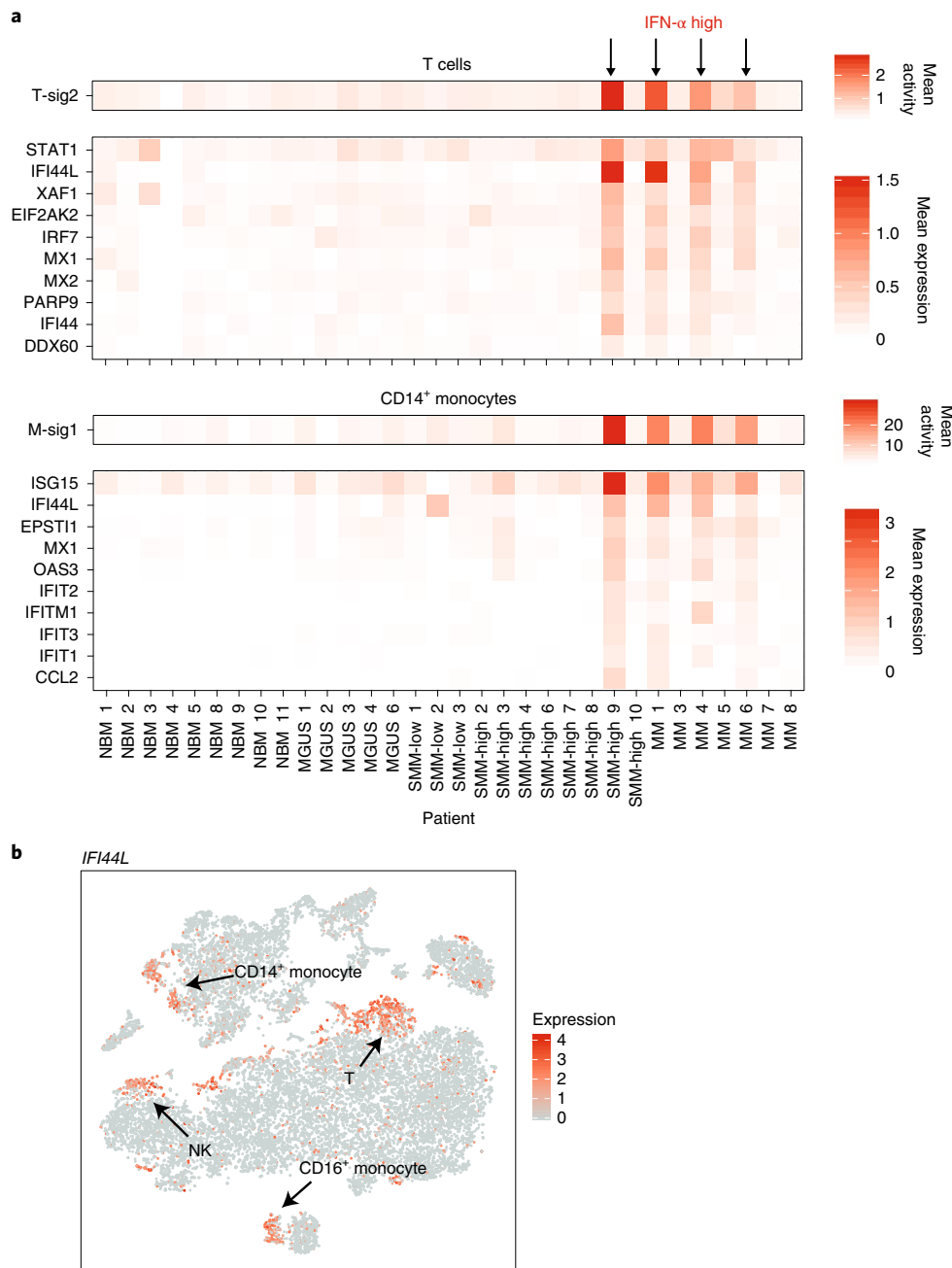


Fig. 4 | IFN type I target genes are upregulated in patients compared to healthy donors. **a**, Mean T-sig2 and M-sig1 cell signature activity across samples, and mean expression of genes most highly weighted in these signatures. **b**, t-SNE representation of cells colored by *IFI44L* expression.

the SMM and MM stages presented a striking shift to T-sig4 ($P=3.1\times 10^{-4}$, d.f.=27.9, $n=30$, Fig. 3c), suggesting a depletion of memory CD8⁺ T cells later during disease progression. In support of this result, we observed in our CyTOF data a twofold decrease in memory CD8⁺ cells in the BM aspirates of patients with SMM (central memory and effector memory T cells, GrA⁺GrB⁻; Fig. 3d and Extended Data Fig. 4a).

We next examined whether these populations displayed the characteristics of T-cell exhaustion. Of four key markers of exhaustion (*PDCD1*, *HAVCR2*, *LAG3* and *TIGIT*), we found that only *LAG3* and *TIGIT* were expressed at detectable levels and were relatively specific to the cytotoxic subsets (with the exception of *TIGIT* expression on T_{reg} cells; Extended Data Fig. 4b). Across cytotoxic T cells, we did not see a difference between healthy individuals and patients in the expression of these genes (Extended Data Fig. 4c).

However, since healthy donor samples primarily were composed of GrK⁺ cytotoxic subsets, we cannot reliably compare the expression of specifically GrB⁺ subsets, which probably would be the relevant subsets to display classical exhaustion.

Of note, in our CyTOF data, we observed significantly higher expression of the checkpoint receptor programmed cell death protein 1 (PD-1) on memory cells in healthy individuals than in patients with SMM (Extended Data Fig. 4d,e, $P=0.047$). Recent publications have connected the expression of PD-1 at the early stages of T-cell differentiation with a mechanism for T-cell activation to balance effector and memory responses^{43,44}, however, its role in MM remains to be elucidated.

Notably, the degree of the shift from memory to effector was variable, and in several samples, such as MM-7, it was completely absent. We did not observe any correlation between

plasma cell cytogenetics and types of cells composing the cytotoxic T-cell cluster.

To address the role of GrK-expressing cytotoxic memory cells in MM progression, we performed *in vivo* assays using syngeneic transplantable myeloma mice with different maturation stages of the memory cell pool. For this, 10-week-old KaLwRij mice with impaired memory cell function and fully immunocompetent older animals (1.5 years old) were injected with 5TGM1 MM cells. Young mice with impaired memory cells showed significantly shorter survival than older animals (Fig. 3e). In a similar assay with C57BL/6J mice injected with Vκ⁺MYC MM cells, we observed early accumulation of plasma cells in the spleen and faster abundance of monoclonal proteins in the blood of younger animals (Fig. 3f,g). However, no difference in survival of myeloma-injected mice was obtained when animal groups with fully established memory cell pool were compared (6-month-old versus 1.5-year-old KaLwRij mice; Fig. 3e, right panel), providing compelling evidence for a previously undetermined critical role of memory cells for immunosurveillance against MM. Future studies in age-matched mice are necessary to further eliminate potential age-associated confounding factors.

IFN response is seen across immune cell types in late-stage disease. The T-sig2 signature was highly enriched for IFN-responsive genes (for example, *STAT1*, *IFI44L* and *ISG15*) and uniquely present in a subset of late-stage patients (Fig. 4a). Likewise, signature analysis in CD14⁺ monocytes isolated an expression program (M-sig1) with highly overlapping marker genes. This signature was present in precisely the same samples, suggesting a common response to the external signals. Indeed, when we visualized expression of the top genes, we observed IFN response in subpopulations of different cell types, including NK, nonclassical monocytes and small numbers of B cells (Fig. 4b). While this signature was strongly present in 4 out of 23 samples, which means we are underpowered to directly link it to myeloma progression (Fisher exact test, $P=0.054$, $n=27$), we have shown in previous work that IFN signaling is significantly upregulated in malignant plasma cells²⁷. Interrogating a publicly available dataset from CD138-enriched plasma cells at different stages of the MM disease ($n=147$) and healthy donors ($n=15$, GSE6477) for the expression of *ISG15* and *MX1*, which scored highly in gene signature analyses in our single-cell data, we found a significantly increased expression of these genes throughout MM progression (Extended Data Fig. 5). Thus, our data from the immune microenvironment provide evidence that signaling in this context occurs not just in myeloma cells, but across immune populations.

CD14⁺ monocytes in the MM microenvironment show defective antigen presentation due to intracellular accumulation of human leukocyte antigen DR isotype (HLA-DR). In addition to the IFN signature found in CD14⁺ monocytes, we discovered that the M-sig2 signature was significantly upregulated in all malignant cases (t -test, $n=30$, d.f.=19.7, $q=1.3 \times 10^{-6}$). The majority of genes highly contributing to this signature were encoding the MHC class II cell surface receptor (*HLA-DRA*, *HLA-DPB1*, *HLA-DRB1* and *HLA-DPA1*; $q \leq 2 \times 10^{-4}$; Fig. 5a and Extended Data Fig. 6a). Expression of MHC class II encoding genes individually was significantly upregulated in CD14⁺ monocytes/macrophages across all disease stages, including MGUS (Fig. 5a and Extended Data Fig. 6a). The mRNA levels of MHC class II receptors together with the expression of IFN-activated genes predominantly determined the organization of CD14⁺ monocytic subclusters (Extended Data Fig. 6b). Additional subclusters were built from individual patients with high expression of the mannose receptor C-type 1 (*MRC1*), *CCL3/4* and CCAAT/enhancer binding protein signaling (Extended Data Fig. 6b).

However, study of MHC class II expression using CyTOF revealed that despite elevated mRNA levels, CD14⁺ cells from patients with SMM and MM exhibited significantly lower HLA-DR surface expression compared to those from healthy donors (Fig. 5b), suggesting pathway dysregulation yet resulting in compromised antigen presentation in these cells. To elucidate whether this change in expression represented a shift in cell subpopulations (for example, MDSCs are known to have low levels of MHC class II surface presentation) or a phenotypic change specifically induced by the myeloma cells, we cocultured CD14⁺ cells isolated from the peripheral blood of healthy donors with MM.1S or RPMI 8226 myeloma cells and analyzed *HLA-DRA* mRNA and HLA-DR and HLA-DP surface expression levels. Indeed, while quantitative reverse-transcription PCR showed a significant increase of *HLA-DRA* mRNA in monocytes cocultured with MM cells, as compared to coculture with CD19⁺ control cells (Extended Data Fig. 7a), a dramatic drop in the surface expression of both HLA-DR and HLA-DP molecules was observed (Fig. 5c, left panel). However, the proportion of CD14⁺ cells expressing HLA-DR and HLA-DP intracellularly remained similar or slightly lower compared to that in controls (Fig. 5c, right panel). We observed intracellular accumulation of HLA-DR in CD14-expressing cells in tissue microarray (TMA) slides of patients with MM compared to membrane-bound HLA-DR in CD14 monocytes from healthy donors (Fig. 5d and Extended Data Fig. 7b). Taken together, our results suggest that MM

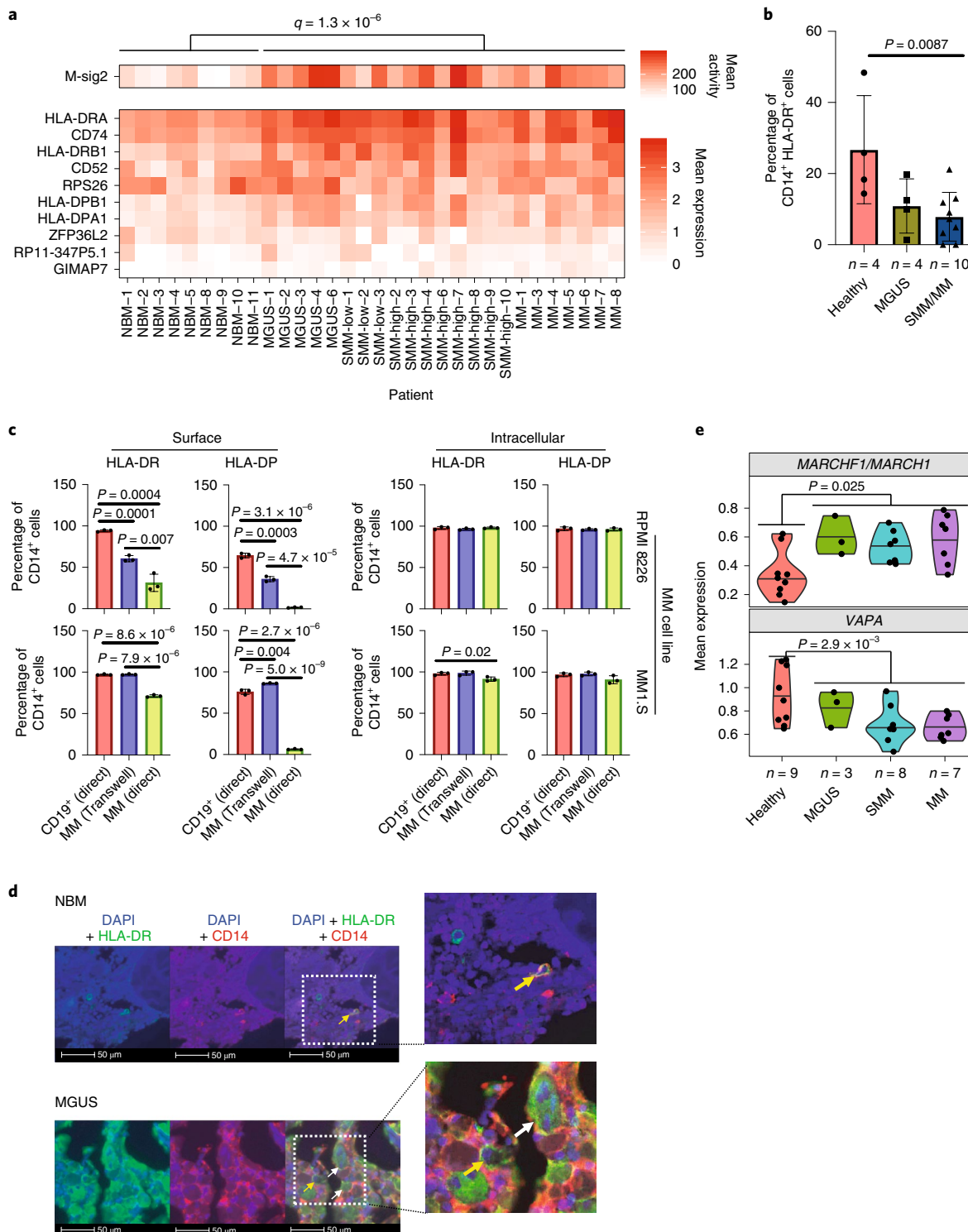
Fig. 5 | Dysregulation of MHC class II in CD14⁺ monocytes in the MM environment. **a**, Mean activity of MHC class II gene signature (M-sig2) and mean expression of these genes across the samples, grouped by stage of progression. Significance was tested by a Benjamini-Hochberg-corrected, two-tailed t -test with d.f.=19.7 on $n=30$ patient samples with at least ten CD14⁺ monocytes. **b**, HLA-DR cell surface protein expression measured by CyTOF across samples. Significantly lower levels of HLA-DR molecules were observed on the surface of CD14⁺ monocytes/macrophages in patients (SMM and MM samples) compared to healthy donors (NBM), with median values of 26.7 for NBM, and 10.9 and 7.9 for SMM and MM samples, respectively. The significant difference was tested with a two-tailed t -test; the bars represent the s.d. **c**, Myeloma cells significantly downregulated surface representation of MHC class II on CD14⁺ monocytes after direct coculture. Human CD14⁺ monocytes were isolated from the blood of healthy donors and cocultured with CD19⁺ B cells or MM1.S and RPMI 8226 myeloma cells. FACS analysis was performed on day 3 of coculture. The median values for surface expression on CD14⁺ cells cocultured with CD19⁺ cells or with RPMI 8226 cells in Transwells or direct coculture were 94.2, 60.4 and 31.3 for HLA-DR and 64.6, 35.9 and 1.7 for HLA-DP, respectively. The median values of 97.0, 97.2 and 91.2 for HLA-DR and 75.8, 86.2 and 6.4 for HLA-DP were detected on the surface of CD14⁺ cells after similar experimental settings with MM1.S cells. The median proportion of CD14⁺ cells expressing HLA-DR intracellularly was 97.8, 96.4 and 98.0; 96.7, 95.9 and 96.0 for HLA-DP in coculture with RPMI 8226; 97.9, 98.6 and 91.9 for HLA-DR; and 96.8, 97.8 and 90.9 for HLA-DP in coculture with MM1.S cells, respectively. The experiment was performed with three independent donors for two different cell lines in triplicate. Significance was derived from the technical replicates, but different donors demonstrated similar loss of HLA-DR expression to that in controls (two-sided t -test; the error bars indicate the s.d.). **d**, Immunofluorescence staining of TMAs from patients with MGUS demonstrates intracellular accumulation of HLA-DR (green) in CD14-expressing monocytes (red) compared to membrane-bound localization of HLA-DR in healthy BM monocytes (BM TMAs of patients with MGUS, SMM and MM ($n=45$, performed in triplicate, total of 135 BM sections; the yellow arrows point to cells with HLA-DR localized to the cell membrane, the white arrows point to cells with HLA-DR accumulated in the cytoplasm). **e**, Upregulated *MARCH1* expression and decreased VAPA levels in CD14⁺ cells from the BM of patients with MM, compared to healthy donors. The violin plots show the minimum, medium and maximum values. A Benjamini-Hochberg-corrected, two-tailed t -test was performed on $n=27$ patient samples with ≥ 50 CD14⁺ monocytes.

cells induce internalization of MHC class II in CD14⁺ cells, reducing their potential for antigen presentation.

Looking for the alterations in the expression of genes responsible for the posttranslational control of MHC class II, we found the gene encoding the E3 ubiquitin protein ligase *MARCHF1/MARCH1* to be progressively upregulated in patients compared to healthy individuals ($P=0.008$) and found decreased levels of the gene encoding ER-resident protein VAMP-associated protein A (VAPA), which plays a role in the inward transport of MHC class II ($P=0.01$, Fig. 5e). By treating CD14⁺ cells

cocultured with MM cell lines with anti-*MARCHF1/MARCH1* small interfering RNAs (siRNAs), we rescued HLA-DR surface presentation (Extended Data Fig. 8). Thus, our results suggest that the upregulation of *MARCHF1/MARCH1* observed in our single-cell RNA dataset could indeed lead to internalization of MHC class II in monocytes in the MM microenvironment.

CD14⁺ monocytes in the MM microenvironment can promote proliferation of myeloma cells and suppress T-cell activation. Since CD14⁺CD11b⁺HLA-DR^{low} cells have been previously defined



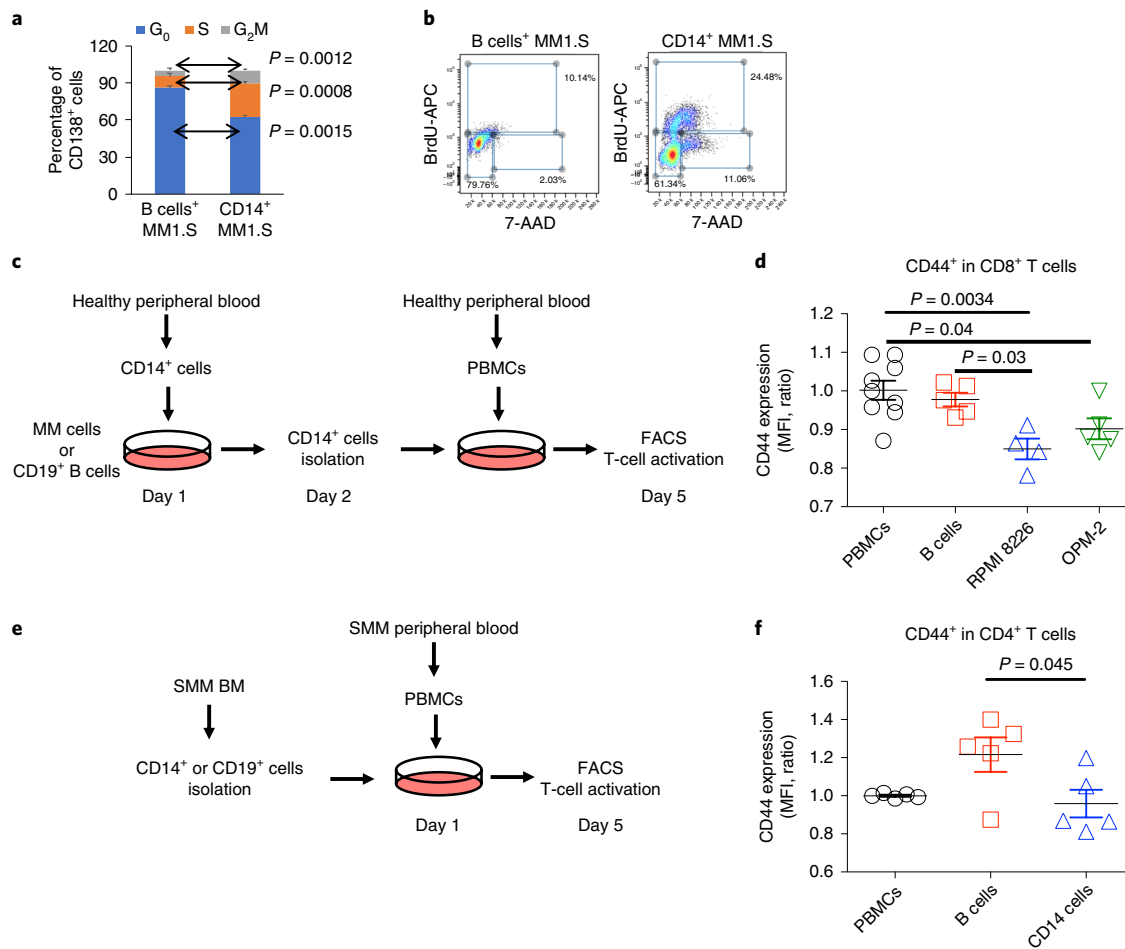


Fig. 6 | CD14-expressing monocytes from the myeloma environment can enhance proliferation of myeloma cells and suppress T-cell activation.

a, Proportion of MM1.S cells in the G₀, S and G₂M cell cycle phases assessed from the frequency of myeloma cells that incorporated BrdU into cellular DNA in the presence of CD14⁺HLA-DR^{low} monocytes or B cells. The median values for MM1.S cells in the G₀, S and G₂M phase of the cell cycle were 86.1, 9.3 and 4.6 for controls cocultured with B cells compared to 62.4, 27.1 and 10.6 for coculture with CD14⁺HLA-DR^{low} cells. The error bars indicate the average deviation. Representative data from one out of three independent experiments performed with three healthy donors. **b**, Representative FACS profiles show the distribution of MM cells in the different cell cycle phases. **c**, Experimental design for the T-cell activation assay of CD14⁺ cells from the MM environment. CD14⁺ cells isolated from the peripheral blood of healthy donors were cocultured with MM cell lines or healthy B cells as a control. The next day, CD14⁺ cells were isolated from the MM coculture and placed into culture with healthy PBMCs. On day 5, activation of T cells was analyzed using FACS. **d**, CD8⁺ T cells cocultured with CD14⁺ cells preconditioned with RPMI 8226 myeloma cells show decreased levels of CD44 compared to those in controls precultured with B cells. The mean fluorescence intensity (MFI) for the PBMC controls was 1.0 compared to 0.98 for B cells, 0.85 for RPMI 8226 cells and 0.9 for OPM-2 cells. One-way ANOVA and Tukey multiple comparison tests were used to test significant differences between groups; statistics were derived from three independent experiments performed in duplicate; the bars indicate the s.d. **e**, Experimental design for T-cell activation assay of CD14⁺ cells from patients with SMM. CD14⁺ or B cells isolated from the BM of patients with SMM were cocultured with PBMCs. On day 5, activation of T cells was analyzed using FACS. **f**, CD4⁺ T cells cocultured with CD14⁺ cells from patients with SMM show decreased levels of CD44 compared to those in controls. The MFI for PBMC controls was 1.0 as compared to 1.2 for B cells and 0.96 for CD14⁺ SMM cells. One-way ANOVA and Tukey multiple comparison tests were used to test significant differences between groups; statistics were derived from three independent experiments performed in duplicate; the bars indicate s.d.

as one of the subsets of monocytic MDSCs (mMDSC), we wanted to further characterize the CD14⁺HLA-DR^{low} cell population from the MM environment and understand its role in myeloma progression and immune suppression. According to our sequencing results, the population of CD14⁺ cells expressed CD11b at levels similar to those in healthy cells. Likewise, it expressed various markers that define mature macrophages, such as CD86, CD163 and CD68, with highly elevated CD206 in one patient (Extended Data Fig. 9a). According to suggested guidelines for the characterization of MDSCs¹⁵, we did not observe increased expression of MDSC-associated genes in patients relative to healthy donors (Extended Data Fig. 9b). Furthermore, CD14⁺ cells from healthy donors after coculture

with MM cells expressed inducible nitric oxide synthase, CD206 and CD163 and did not polarize toward the Lin⁻CD11b⁺CD33⁺ mMDSC phenotype (Extended Data Fig. 9c). Thus, while this cell population may overlap with CD14⁺CD11b⁺HLA-DR^{low} populations termed mMDSCs described in other studies, our results agree with the observation of others that additional markers are needed to isolate myeloid cells with a specific mMDSC phenotype.

Interestingly, after coculture of myeloma cell lines (MM1.S, RPMI 8226, OPM-2, KMS-18) with CD14⁺HLA-DR^{low} cells, we observed significant changes in the cell cycle of MM1.S cells resulting in a significantly increased fraction of cells in the S ($P=0.006$) and G₂M ($P=0.0012$) phases of the cell cycle, as compared to that in

control cells, indicating that CD14⁺HLA-DR^{low} cells can accelerate the proliferation of MM cells (Fig. 6a,b).

Then, we tested the ability of CD14⁺ cells from the MM environment to alter T-cell activity. We assessed the expression of the CD44 activation marker in T cells after coculture with CD14⁺ cells that were preconditioned with MM cells (Fig. 6c). In contrast to B-cell controls, CD8⁺ cells after coculture with CD14⁺ monocytes from the MM environment showed reduced expression of CD44 (Fig. 6d), indicating suppression of T-cell activation. In a similar experiment with peripheral blood mononuclear cells (PBMCs) cocultured with either CD14⁺ cells or CD19⁺ B cells isolated from the BM aspirates of patients with SMM (Fig. 6e), we observed downregulation of CD44 in CD4⁺ T cells cocultured with CD14⁺ cells (Fig. 6f).

Altogether, these results indicate that CD14⁺HLA-DR^{low} cells from the myeloma environment can accelerate proliferation of MM cells and exhibit suppressive activity by inhibiting T-cell activation.

Discussion

Myeloma is an incurable disease that can cause irreversible organ damage. Early intervention represents an attractive alternative for treatment, although we cannot accurately predict which patients with MGUS/SMM will progress. Further understanding of disease progression requires comprehensive molecular characterization, including that of the tumor's microenvironment and the host's immune response. In this study, we used single-cell RNA-seq (scRNA-seq) of patient samples across all stages of MM to elucidate the transcriptomic alterations within the immune microenvironment along disease progression.

Through analysis of the cellular composition of the tumor microenvironment, we showed a significant, albeit heterogeneous, enrichment of T cells, CD16⁺ monocytes and NK cells established at the MGUS stage of the disease, indicating an early launch of an immune response. Indeed, expansion of T and NK cells in the peripheral blood and BM of patients with hematopoietic malignancies, including MM, has been reported previously^{23–25,46–48} and has been associated with improved outcomes in MM^{33,38,49,50}. Using scRNA-seq, we characterized the subtypes and expression states of these populations.

Our analysis further revealed that in patients with high NK-cell infiltration, this fraction is predominantly composed of CXCR4-expressing cells, while samples with fewer NK cells have a shift toward CX3CR1 expression. Previous studies have shown that these receptors are responsible for chemotaxis, mediating homing to the BM or facilitating BM egress³⁹. If in certain subsets MM may initiate the egress of NK cells into the circulation⁵¹, this may explain the heterogeneous frequency of NK cells observed in our data and could suggest an MM-orchestrated mechanism of immune evasion.

Interrogation of the cytotoxic compartment demonstrates that, starting from SMM, there is a loss of memory cells with considerable skewing of T-cell differentiation toward the GrB/H-expressing effector state. From our *in vivo* results, we demonstrate the previously unrecognized pivotal role of memory cells in the immune response against tumor cells. It is important to note that the proportion of the effector cell subtypes did not correlate with the cytogenetic characteristics of the tumor. Individual subpopulations of cytotoxic effectors, including NK T cells, gamma delta T cells, CD4⁺ and CD8⁺ effector cells are well described and their functionality in MM is under extensive investigation. In MM, these cytotoxic cells often exhibit either suppressed phenotype (as CD8⁺ T cells⁵²) or anergy (as in gamma delta T cells⁵³) and impaired functionality as reported for NK T cells⁵⁴, and several approaches have been tested to overcome this dysregulation^{55,56}.

The immunosuppressive role of MDSCs, CD14⁺HLA-DR^{low/neg} cells from the monocytic lineage, has been previously established in lymphoma, glioblastoma, prostate cancer, renal cell carcinoma

and MM^{29,57–59}. Our data demonstrate that in addition to MDSCs, mature CD14⁺ monocytes/macrophages also undergo a phenotypic shift leading to loss of MHC class II surface representation as early as in the MGUS stage. These CD14⁺ cells with compromised MHC class II representation acquire immunosuppressive potential and can suppress T-cell activation. We demonstrated that overexpression of *MARCHF1/MARCH1* contributes to the internalization of MHC class II proteins. Importantly, this condition can be rescued by down-regulating *MARCHF1/MARCH1* expression, offering a potential for therapeutic interventions. Overall, this signaling was impaired in the majority of patients already at the early precursor MGUS stage, indicating that monocytes/macrophages are very sensitive to the MM-directed shaping of a permissive tumor microenvironment.

Extensive coregulatory networks have been described in the tumor microenvironment, whereby tumor cells regulate the stromal and immune microenvironment and vice versa, all in support of tumor growth and dissemination^{16,17}. We have previously demonstrated that IFN type I secreted from MM cells promotes immunosuppression, which favors MM growth⁶⁰. In this study, we found highly upregulated IFN signaling across immune subsets. Thus, our results further implicate IFN signaling in MM and indicate that such a complex regulatory network could already be in place at the high-risk SMM stage of disease, identifying it as a potential target for therapeutic intervention to prevent progression.

We profiled sequential immune alterations occurring during MM progression, beginning at the earliest stage (Extended Data Fig. 10). MM represents a unique setting with a readily detectable premalignant stage; observing early immune alterations in response to a neoplastic environment raises the possibility of similar mechanisms appearing in the precursors of other cancers. It is our hope that understanding this evolution of the myeloma microenvironment will provide new targets for therapeutic approaches, and that leveraging inter-patient heterogeneity will enable stratification of patients by risk of progression and create the opportunity for early intervention.

Methods

Patient samples and cell preparation. Primary peripheral blood cells or BM samples from patients with MGUS, SMM or MM, as well as healthy donors were collected at the Dana-Farber Cancer Institute. These studies were approved by the Dana-Farber Cancer Institute Institutional Review Board. Informed consent was obtained from all patients and healthy volunteers in accordance with the Declaration of Helsinki protocol (fifth revision from 2000 with Clarifications of Articles 29, 30 (2002–2004), and the most recent iteration from 2013). CD138[−] or CD45⁺ BM cell fractions were isolated using magnetic-activated cell sorting technology (Miltenyi Biotec). Selected cells were either viably cryopreserved in dimethylsulfoxide at a final concentration of 10% or used immediately for scRNA-seq.

Human MM.1S and RPMI 8226 cells were purchased from ATCC, while the KMS-18 myeloma cell line was obtained from the Japanese Collection of Research Bioresources and the OPM-2 cell line was obtained from DSMZ. For the *in vitro* experiments, these cell lines were cultured in Roswell Park Memorial Institute (RPMI) 1640 medium containing 10% fetal calf serum (Sigma-Aldrich), 2 mM of L-glutamine, 100 U ml^{−1} penicillin and 100 µg ml^{−1} streptomycin (Gibco).

Sequencing library construction using the 10x Genomics platform. Frozen BM cells were rapidly thawed, washed, counted and resuspended in PBS and 0.04% bovine serum albumin to a final concentration of 1,000 cells per µl. The Chromium Controller (10x Genomics) was used for parallel sample partitioning and molecular barcoding⁶¹. To generate a single-cell Gel Bead in EMulsion, cellular suspensions were loaded on a Single Cell 3' chip together with the Single Cell 3' Gel Beads, according to the manufacturer's instructions (10x Genomics). scRNA-seq libraries were prepared using the Chromium Single Cell 3' Library Kit v.2 (10x Genomics). Fourteen cycles were used for the total complementary DNA amplification reaction and for the total sample index PCR. Generated libraries were combined according to Illumina specifications and paired-end sequenced on HiSeq 2500/4000 platforms with standard Illumina sequencing primers for both sequencing and index reads; 100 cycles were used to sequence Read1 and Read2.

Preprocessing of scRNA-seq data. Sample demultiplexing, barcode processing, alignment to the human genome (hg38) and single-cell 3' gene counting was performed using the Cell Ranger Single-Cell Software Suite v.2.0.1. Cells called by

Cell Ranger were further filtered to those with <10% mitochondrial expression, >200 genes covered and >600 total unique molecular identifiers. Expression values were calculated as:

$$e_{g,c} = \log\left(\frac{10^4}{N_c} n_{g,c} + 1\right)$$

for a cell c with N_c total unique molecular identifiers, $n_{g,c}$ of which map to gene g .

Separation of plasma and immune cell populations. To remove cells incorrectly sorted during bead selection (that is, plasma cells in the CD138⁻ fractions), we first performed coarse clustering of the data including all cells. We selected 2,744 genes with high expression and dispersion, excluding genes on the sex chromosomes, and z -normalized the data after regressing out variation due to total number of unique molecular identifiers or percentage mitochondrial RNA in each cell. We then performed Seurat k -nearest neighbors clustering with resolution 0.6 on the first 20 principal components of the resulting data. A plasma cell score was calculated for each cluster as the mean expression of CD138 (*SDCI*), CD319 (*SLAMF7*) and BCMA (*TNFRSF17*); clusters with a score of >1 were identified as plasma cell clusters. Clusters with >4 mean *HBA1* expression were deemed to be erythroid clusters, and cells in these clusters were excluded from future analyses. Cells originating from the CD138⁻ fraction in nonplasma, nonerythroid clusters formed our immune cell dataset.

Gene selection. When selecting genes for downstream analysis, we excluded genes with high potential to be influenced by cross-cell contamination effects. 10x technology exhibits low rates of mRNAs associated with the barcodes of cells from which they did not originate, possibly from sources such as extracellular mRNAs captured in the droplet. While in the vast majority of cases this is undetectable, for ultra-highly expressed genes such as immunoglobulins, the contributions can become noticeable. Thus, we excluded genes that were drastically higher in expression for the excluded compartments (plasma cells and erythroid cells).

In addition, we filtered genes found to have a strong sex bias in our data. For the purposes of clustering analyses, we removed all genes from the sex chromosomes to avoid any cumulative effects that could separate samples based on sex. For downstream gene- or signature-level analyses, so as not to lose informative genes on the X chromosome, we only excluded genes found to have a statistically significant sex bias (two-sample t -test on mean gene expression at a false discovery rate threshold of 10%).

Analysis of immune cell populations. A total of 2,100 variably expressed genes were identified using the filtering procedure described earlier and the same expression and dispersion criteria as in the analysis of principal components. Clusters were identified using Seurat k -nearest neighbors clustering with resolution 1.4 on the first 20 principal components of the z -normalized data. Cell types were then identified for each cluster by examining the expression of marker genes, as well as the top differentially expressed genes, in each cluster. Cells were visualized by t -distributed stochastic neighbor embedding (*t*-SNE) on the same 20 principal components.

Nonnegative matrix factorization (NMF)-derived gene expression signatures. We defined gene expression signatures for T cells and CD14⁺ monocytes using our SignatureAnalyzer-GPU⁶² tool (<https://github.com/broadinstitute/SignatureAnalyzer-GPU>), which implements a previously described Bayesian NMF algorithm⁶³. This method approximates the expression profile of each cell (represented as a column in the input matrix) as an additive combination of latent expression programs (each column in the W -matrix output), each with an associated weight or ‘activity’ in each cell given by the H -matrix. This Bayesian variant of NMF encourages sparse interpretable solutions by imposing an exponential prior distribution on the weights of the W - and H -matrices and allows automatic discovery of the number of signatures required to explain the data.

After signature discovery, the columns of W were normalized to a sum of 1 and all the weight was shifted into the H -matrix:

$$W'_{g,k} = \frac{W_{g,k}}{\sum_{g'=1}^G W_{g',k}}$$

$$H'_{k,p} = \left(\sum_{g=1}^G W_{g,k} \right) H_{k,p}$$

for gene g (out of G total genes), signature k and patient p . Signatures significantly altered between disease states were identified by calculating the mean signature activity for each patient and performing a two-sample t -test, reporting results below a 10% Benjamini–Hochberg false discovery rate level. Marker genes for each signature were identified by sorting genes according to their relative contribution to each signature:

$$\frac{W_{g,k}}{\sum_{k'=1}^K W_{g,k'}}$$

and taking the top 10 genes where the gene contributed at least 1% of the total signature activity.

Analysis of cells by CyTOF. Sample staining for mass cytometry (CyTOF) was performed according to the manufacturer’s guidelines (Fluidigm). Briefly, the CD138⁻ or CD45⁺ populations of BM samples from patients with MM or healthy donors were thawed, washed and barcoded using the Cell-ID 20-Plex Pd Barcoding Kit (Fluidigm). After barcoding, cells were incubated with human Fc Receptor Blocking Reagent (Miltenyi Biotec) and human surface marker antibodies as a single multiplexed sample (Maxpar Human Immune Monitoring Panel Kit, 29-marker panel; Fluidigm). After staining, cells were washed in Maxpar Cell Staining Buffer (Fluidigm), resuspended at the concentration of 1×10^6 cells ml⁻¹ and acquired on a CyTOF Helios mass cytometer (Fluidigm). Downstream analysis of the individual component samples was performed after running the debarcoding application. An automated analysis GemStone MC software (Verity, provided by Maxpar, Fluidigm) was used to clean the data files by automatically identifying and removing cell doublets, debris and dead cells, as well as identifying major immune cell subsets. Expression levels of HLA-DR molecules on the cell surface were analyzed in Cytobank (Cytobank).

To phenotype the Gr-expressing T-cell populations, CyTOF was performed on CD138⁻ cells from the BM aspirates of patients with SMM and healthy donors using TIGIT-143Nd, PD-1-175Lu, TIM3-153Eu (Maxpar) and the Maxpar Human T-Cell Phenotyping Panel Kit, 16 Marker. T-cell subsets were defined as suggested by the manufacturer.

Flow cytometry analysis. Antihuman antibodies against CD138 (clone MI15), CD14 (clone 6D3), HLA-DR (clone L243) were obtained from BioLegend. HLA-DP (clone DP11.1) was obtained from Santa Cruz Biotechnology. iNOS (catalog no. ab115819) was obtained from Abcam. CD33 (catalog no. 303413), CD11b (catalog no. 301341), CD206 (catalog no. 321113), CD163 (catalog no. 33362) and FITC antihuman Lineage Cocktail (catalog no. 348801) were obtained from BioLegend. Antibodies were used for fluorescence-activated cell sorting (FACS) analyses. The LIVE/DEAD Fixable Aqua Dead Cell Stain Kit (Thermo Fisher Scientific) was used for the discrimination of dead cells. Data from the stained samples was acquired using a FACS Canto II Flow Cytometer (BD Biosciences). The results were analyzed in Cytobank (Cytobank).

Myeloma cell coculture assay. Human CD14⁺ monocytes or CD19⁺ B cells were obtained from fresh peripheral blood cells using CD14 and CD19 MicroBeads (Miltenyi Biotec). Briefly, red blood cells were lysed (RBC Lysis Buffer; BioLegend), washed and CD14⁺ and CD19⁺ cell populations were isolated according to the manufacturer’s instructions. CD14⁺ monocytes at 2×10^6 were cocultured with 1×10^6 myeloma cell lines. CD19⁺ B cells were used as a negative control. Transwell-permeable inserts with a pore size of 0.4 μ m were used to prevent cell-cell interactions (Corning). After 3–4 d of coculture, cells were collected and analyzed for HLA-DR expression using flow cytometry or quantitative PCR.

siRNA knockdown of *MARCHF1/MARCH1*. *MARCHF1/MARCH1* knockdown in CD14⁺ cells was performed using anti-*MARCHF1/MARCH1* siRNAs (catalog nos. 127048 and 127049; Thermo Fisher Scientific) and Lipofectamine RNAiMAX Transfection Reagent (Thermo Fisher Scientific) according to the manufacturer’s instructions. Briefly, CD14⁺ monocytes were isolated from the peripheral blood of healthy donors using CD14 MicroBeads (Miltenyi Biotec) and plated into 24-well plates at 0.5×10^6 in 500 μ l; 5 pmol of siRNA was used per well. Silencer Negative Control No. 1 siRNA (catalog no. AM4611; Thermo Fisher Scientific) was used as a negative control. Twelve hours posttransfection, 1×10^6 MM cells were added and cultured for the next 24 h. Cells were collected and analyzed for the HLA-DR and *MARCHF1/MARCH1* expression using flow cytometry or immunofluorescence microscopy.

RNA isolation and quantitative PCR with reverse-transcription (RT-qPCR). mRNA was isolated with the miRNeasy Mini Kit (catalog no. 217004; QIAGEN). Purified RNA was measured by NanoDrop (Thermo Fisher Scientific) and cDNA was synthesized from 500 ng of total RNA using a High-Capacity cDNA Reverse Transcription Kit (catalog no. 4368814; Thermo Fisher Scientific). Expression levels of *HLA-DRA* were obtained using a TaqMan qPCR assay (Hs.PT.58.14332844) and an actin assay as the internal control (Hs.PT.39a.22214847) from Integrated DNA Technologies. To measure the expression of different *MARCHF1/MARCH1* transcripts, two primer pairs were designed and *MARCHF1/MARCH1* RT-qPCR reactions were prepared using the PowerTrack SYBR Green Master Mix (catalog no. 4367659; Thermo Fisher Scientific). TaqMan and SYBR green reactions were carried out on Quant Studio 7 (Thermo Fisher Scientific). The assays were run in triplicate using CD14⁺ cells isolated from three independent donors. The $\Delta\Delta Ct$ method was used for normalization on the actin and *GAPDH* housekeeping genes. The primer sequences of *MARCHF1/MARCH1* and *GAPDH* were: *MARCHF1/MARCH1* pair 2 forward, 5'-CAGGAGCCAGTCAGGTTGT-3'; *MARCHF1/MARCH1* pair 2 reverse, 5'-AGAGCTCACAGCAGCGTGTA-3'; *MARCHF1/MARCH1* pair 3 forward, 5'-TAATCGGATCACCTGTGTG-3'; *MARCHF1/MARCH1* pair 3 reverse, 5'-GCGCCACAACTGAACATAGA-3';

GAPDH forward, 5'-AGCACATCGCTCAGACAC-3' and GAPDH reverse, 5'-GCCCAATACGACCAAATCC-3'.

5-bromo-2'-deoxyuridine (BrdU) proliferation assay. MM cells were cocultured with CD14⁺ monocytes isolated from the PBMCs of healthy donors for 48 h. MM cells cocultured with CD19⁺ B cells were used as the control. After coculture, cells were labeled with 1 mM of BrdU for 2 h and then stained with antibodies for surface expression of CD138 (clone MI15) and CD14 (clone 6D3). After this, cells were fixed and permeabilized with Cytofix/Cytoperm Buffer according to the manufacturer's protocol (catalog no. 552598; BD Biosciences) before staining with allophycocyanin (APC)-conjugated anti-BrdU for 20 min. Total DNA was stained using a 7-AAD solution (catalog no. 555816, BD Biosciences). The cell cycle of CD138⁺ MM cells was analyzed using flow cytometry.

Mixed lymphocyte reaction. The mixed lymphocyte reaction was performed in duplicate in 96-well, round-bottom plates (catalog no. 7007; Corning). PBMCs were cultured in the RPMI 1640 medium (Gibco, 11875) supplemented with 100 U ml⁻¹ of penicillin-streptomycin (catalog no. 15140122; Gibco), 10% (vol/vol) fetal calf serum (catalog no. A31604; Gibco) and 50 µM of 2-mercaptoethanol (catalog no. M6250; Sigma-Aldrich), 2 mM of L-glutamine (catalog no. 25030081; Gibco) for 3 d at 37 °C in 5% CO₂ in air. Cells were stimulated with 4 µg ml⁻¹ of antihuman CD3 antibody (clone OKT3, catalog no. 317302; BioLegend), 4 µg ml⁻¹ antihuman CD28 antibody (clone CD28.2, catalog no. 302902; BioLegend) and 200 ng of recombinant human IL-2 (catalog no. 200-02; PeproTech).

CD14⁺ cells were isolated from healthy PBMCs and cocultured with either MM cell lines (OPM-2, MM1.S) or healthy CD19⁺ B cells for 24 h in a 1:2 ratio. After 24 h, CD14⁺ cells were isolated and added as modulators to the freshly isolated PBMCs from healthy donors. The cell number of responder versus modulator cells was 1 × 10⁵:8 × 10³ in the final volume of 200 µl per well. PBMCs without modulator cells served as a reaction system control. In the second experimental setup, CD14⁺ or CD19⁺ cells isolated from fresh BM aspirate of a patient with SMM were used as modulators and PBMCs from the same patient were used as responders. Cells were collected at days 3–5 for flow cytometry (FACSCanto II; BD Biosciences). The LIVE/DEAD Fixable Green Dead Cell Stain Kit (catalog no. L23101; Thermo Fisher Scientific) was used to gate out the dead cells. The antibodies used in this experiment were (all BioLegend): PerCP/Cy5.5 antihuman CD4 (clone OKT4; catalog no. 317428); Brilliant Violet 510 anti-mouse/human CD44 (clone IM7, catalog no. 103044); APC/Cy7 antihuman CD8a (clone HIT8a; catalog no. 300926).

Immunohistochemistry and immunofluorescence. Formalin-fixed paraffin-embedded tissue sections were baked in an Isotemp Oven at 60 °C for 30 min to melt excess paraffin. Tumor sections were stained with BOND RX Autostainer (Leica Biosystems) using the BOND Polymer Refine Detection Kit (catalog no. DS9800; Leica Biosystems). Antigen retrieval was performed with the BOND Epitope Retrieval Solution 1 (citrate, pH = 6.0; Leica Biosystems) for 30 min. Dual-immunohistochemistry staining was performed using anti-CD14 (1:100, clone D7A2T; Cell Signaling Technology), which was detected by the Alexa Fluor 594 Tyramide Reagent (catalog no. B40957; Thermo Fisher Scientific) and anti-HLA-DR (1:500, clone TAL.1B5; Dako) detected by Alexa Fluor 488 Tyramide Reagent (catalog no. B40953; Thermo Fisher Scientific). NucBlue Fixed Cell ReadyProbes Reagent (DAPI; catalog no. R37606; Thermo Fisher Scientific) was used as the background stain.

For cytospins, CD14⁺ cells transfected with siRNA and cocultured with MM cells for 24 h were purified using flow cytometry. Cells were fixed with 4% paraformaldehyde, washed with PBS and diluted to no more than 0.5 × 10⁶ cells ml⁻¹. Then, 100 µl of cell suspension was loaded into a cuvette with the slides mounted with the paper pad. The cuvette was placed into a metal holder and centrifuged at 800 r.p.m. for 5 min. After centrifugation, cells were immediately fixed, permeabilized with Cytofix/Cytoperm buffer and incubated with primary antibodies for MARCHF1/MARCH1 (1:100, catalog no. PA5-53199; Thermo Fisher Scientific) and HLA-DR (1:100, catalog no. 307602; BioLegend) for 1 h. Slides were washed for 15 min in PBS and incubated with corresponding secondary antibodies (Abcam) for 1 h. Post-incubation, slides were washed twice and mounted using DAPI mounting solution (Dako).

In vivo assays. C57BL/6 mice were purchased from The Jackson Laboratory. C57BL/KalwRij mice were purchased from Harlan Laboratories. All mice were treated, monitored and euthanized in accordance with the approved protocol of the Dana-Farber Cancer Institute Animal Care and Use Committee; 4 × 10⁶ 5TGM1 cells were injected intravenously into C57BL/KalwRij mice for survival studies, while 4 × 10⁶ VK*MYC cells were injected intravenously into C57BL/6 mice for monoclonal protein secretion (M spike) and plasma cell infiltration analyses. At 3 weeks postinjection, BM cells and peripheral blood were collected. BM cells were obtained through flushing of femurs with 1× PBS. The proportion of CD138⁺ plasma cells was determined after cell staining with the APC anti-mouse CD138 antibody (catalog no. 142505; BioLegend) by flow cytometry. An M spike analysis was performed with 1 µl of blood serum using QuickGel electrophoresis (Helena Laboratories).

Statistical analysis of in vivo and in vitro studies. One-way analysis of variance (ANOVA) and Tukey multiple comparison test were used when three or more independent groups were compared. An unpaired Student's *t*-test was used to compare two independent groups. All tests were two-tailed. The log-rank test was used to analyze survival data. *P*<0.05 was considered statistically significant.

Statistics and reproducibility. No statistical method was used to predetermine sample size. Samples with insufficient numbers of cells or library complexity were excluded from the analyses. Investigators were not blinded to the study of human sequencing data.

Reporting Summary. Further information on research design is available in the Nature Research Reporting Summary linked to this article.

Data availability

The scRNA-seq data that support the findings of this study have been deposited with the Gene Expression Omnibus under accession code GSE124310. Raw sequencing data have been deposited with the database of Genotypes and Phenotypes (phs001323.v1.p1). Previously published microarray data that were reanalyzed in this study are available under accession code GSE6477. Source data for Figs. 1–6 and Extended Data Figs. 2–4 and 6–9 have been provided in corresponding Source Data tables. All other data supporting the findings of this study are available from the corresponding author upon reasonable request.

Code availability

The single-cell RNA data was processed using cellranger v.2.0.1 (<https://www.10xgenomics.com/>) and analyzed with the R package Seurat v.2.3.1 (<https://satijalab.org/seurat/>). Gene expression signatures were extracted using our SignatureAnalyzer algorithm available on github (<https://github.com/broadinstitute/getzlab-SignatureAnalyzer>).

Received: 30 October 2019; Accepted: 10 March 2020;

Published online: 27 April 2020

References

- Kyle, R. A. & Rajkumar, S. V. Multiple myeloma. *Blood* **111**, 2962–2972 (2008).
- Landgren, O. Monoclonal gammopathy of undetermined significance and smoldering multiple myeloma: biological insights and early treatment strategies. *Hematology Am. Soc. Hematol. Educ. Program* **2013**, 478–487 (2013).
- Rajkumar, S. V. Multiple myeloma: 2011 update on diagnosis, risk-stratification, and management. *Am. J. Hematol.* **86**, 57–65 (2011).
- Kyle, R. A. et al. Monoclonal gammopathy of undetermined significance (MGUS) and smoldering (asymptomatic) multiple myeloma: IMWG consensus perspectives risk factors for progression and guidelines for monitoring and management. *Leukemia* **24**, 1121–1127 (2010).
- Rajkumar, S. V. et al. Serum free light chain ratio is an independent risk factor for progression in monoclonal gammopathy of undetermined significance. *Blood* **106**, 812–817 (2005).
- Rajkumar, S. V. et al. Impact of primary molecular cytogenetic abnormalities and risk of progression in smoldering multiple myeloma. *Leukemia* **27**, 1738–1744 (2013).
- Hanamura, I. et al. Frequent gain of chromosome band 1q21 in plasma-cell dyscrasias detected by fluorescence in situ hybridization: incidence increases from MGUS to relapsed myeloma and is related to prognosis and disease progression following tandem stem-cell transplantation. *Blood* **108**, 1724–1732 (2006).
- Manier, S. et al. Genomic complexity of multiple myeloma and its clinical implications. *Nat. Rev. Clin. Oncol.* **14**, 100–113 (2017).
- Bladé, J., Dimopoulos, M., Rosiñol, L., Rajkumar, S. V. & Kyle, R. A. Smoldering (asymptomatic) multiple myeloma: current diagnostic criteria, new predictors of outcome, and follow-up recommendations. *J. Clin. Oncol.* **28**, 690–697 (2010).
- Kyle, R. A. et al. Clinical course and prognosis of smoldering (asymptomatic) multiple myeloma. *N. Engl. J. Med.* **356**, 2582–2590 (2007).
- Landgren, O. et al. Monoclonal gammopathy of undetermined significance (MGUS) consistently precedes multiple myeloma: a prospective study. *Blood* **113**, 5412–5417 (2009).
- Hanahan, D. & Weinberg, R. A. The hallmarks of cancer. *Cell* **100**, 57–70 (2000).
- Tyekucheva, S. et al. Stromal and epithelial transcriptional map of initiation progression and metastatic potential of human prostate cancer. *Nat. Commun.* **8**, 420 (2017).
- Glavey, S. V. et al. Proteomic characterization of human multiple myeloma bone marrow extracellular matrix. *Leukemia* **31**, 2426–2434 (2017).
- El-Haiji, C. P. et al. Critical role for lysyl oxidase in mesenchymal stem cell-driven breast cancer malignancy. *Proc. Natl. Acad. Sci. USA* **109**, 17460–17465 (2012).

16. Pearce, O. M. T. et al. Deconstruction of a metastatic tumor microenvironment reveals a common matrix response in human cancers. *Cancer Discov.* **8**, 304–319 (2018).
17. Finak, G. et al. Stromal gene expression predicts clinical outcome in breast cancer. *Nat. Med.* **14**, 518–527 (2008).
18. Calon, A. et al. Stromal gene expression defines poor-prognosis subtypes in colorectal cancer. *Nat. Genet.* **47**, 320–329 (2015).
19. Petitprez, F. et al. PD-L1 expression and CD8⁺ T-cell infiltrate are associated with clinical progression in patients with node-positive prostate cancer. *Eur. Urol. Focus* **5**, 192–196 (2019).
20. Zhang, L. et al. Intratumoral T cells, recurrence, and survival in epithelial ovarian cancer. *N. Engl. J. Med.* **348**, 203–213 (2003).
21. Podar, K., Hideshima, T., Chauhan, D. & Anderson, K. C. Targeting signalling pathways for the treatment of multiple myeloma. *Expert Opin. Ther. Targets* **9**, 359–381 (2005).
22. Klein, B. Cytokine, cytokine receptors, transduction signals, and oncogenes in human multiple myeloma. *Semin. Hematol.* **32**, 4–19 (1995).
23. Sawanobori, M. et al. Natural killer cell frequency and serum cytokine levels in monoclonal gammopathies: correlation of bone marrow granular lymphocytes to prognosis. *Acta Haematol.* **98**, 150–154 (1997).
24. Pessoa de Magalhães, R. J. et al. Analysis of the immune system of multiple myeloma patients achieving long-term disease control by multidimensional flow cytometry. *Haematologica* **98**, 79–86 (2013).
25. Bailur, J. K. et al. Early alterations in stem-like/resident T cells, innate and myeloid cells in the bone marrow in preneoplastic gammopathy. *JCI Insight* **4**, e127807 (2019).
26. Leone, P. et al. Dendritic cells accumulate in the bone marrow of myeloma patients where they protect tumor plasma cells from CD8⁺ T-cell killing. *Blood* **126**, 1443–1451 (2015).
27. Kawano, Y. et al. Blocking IFNAR1 inhibits multiple myeloma-driven Treg expansion and immunosuppression. *J. Clin. Invest.* **128**, 2487–2499 (2018).
28. Feng, X. et al. Targeting CD38 suppresses induction and function of T regulatory cells to mitigate immunosuppression in multiple myeloma. *Clin. Cancer Res.* **23**, 4290–4300 (2017).
29. Ramachandran, I. R. et al. Myeloid-derived suppressor cells regulate growth of multiple myeloma by inhibiting T cells in bone marrow. *J. Immunol.* **190**, 3815–3823 (2013).
30. Nakamura, K. et al. Dysregulated IL-18 is a key driver of immunosuppression and a possible therapeutic target in the multiple myeloma microenvironment. *Cancer Cell* **33**, 634–648.e5 (2018).
31. Zheng, Y. et al. Macrophages are an abundant component of myeloma microenvironment and protect myeloma cells from chemotherapy drug-induced apoptosis. *Blood* **114**, 3625–3628 (2009).
32. De Beule, N. et al. Tumour-associated macrophage-mediated survival of myeloma cells through STAT3 activation. *J. Pathol.* **241**, 534–546 (2017).
33. Osterborg, A., Nilsson, B., Björkholm, M., Holm, G. & Mellstedt, H. Natural killer cell activity in monoclonal gammopathies: relation to disease activity. *Eur. J. Haematol.* **45**, 153–157 (1990).
34. Scavelli, C. et al. Vasculogenic mimicry by bone marrow macrophages in patients with multiple myeloma. *Oncogene* **27**, 663–674 (2008).
35. Minnie, S. A. et al. Myeloma escape after stem cell transplantation is a consequence of T-cell exhaustion and is prevented by TIGIT blockade. *Blood* **132**, 1675–1688 (2018).
36. Dispenzieri, A. et al. Immunoglobulin free light chain ratio is an independent risk factor for progression of smoldering (asymptomatic) multiple myeloma. *Blood* **111**, 785–789 (2008).
37. Perussia, B. Fc receptors on natural killer cells. *Curr. Top. Microbiol. Immunol.* **230**, 63–88 (1998).
38. Yang, C. et al. Heterogeneity of human bone marrow and blood natural killer cells defined by single-cell transcriptome. *Nat. Commun.* **10**, 3931 (2019).
39. Bernardini, G., Sciumè, G. & Santoni, A. Differential chemotactic receptor requirements for NK cell subset trafficking into bone marrow. *Front. Immunol.* **4**, 12 (2013).
40. Baecher-Allan, C., Wolf, E. & Hafler, D. A. MHC class II expression identifies functionally distinct human regulatory T cells. *J. Immunol.* **176**, 4622–4631 (2006).
41. Karalis, K. et al. Autocrine or paracrine inflammatory actions of corticotropin-releasing hormone in vivo. *Science* **254**, 421–423 (1991).
42. Bratke, K., Kuepper, M., Bade, B., Virchow, J. C. Jr. & Luttmann, W. Differential expression of human granzymes A, B, and K in natural killer cells and during CD8⁺ T cell differentiation in peripheral blood. *Eur. J. Immunol.* **35**, 2608–2616 (2005).
43. Ahn, E. et al. Role of PD-1 during effector CD8 T cell differentiation. *Proc. Natl Acad. Sci. USA* **115**, 4749–4754 (2018).
44. Odorizzi, P. M., Pauken, K. E., Paley, M. A., Sharpe, A. & Wherry, E. J. Genetic absence of PD-1 promotes accumulation of terminally differentiated exhausted CD8⁺ T cells. *J. Exp. Med.* **212**, 1125–1137 (2015).
45. Roccaro, A. M. et al. CXCR4 regulates extra-medullary myeloma through epithelial-mesenchymal-transition-like transcriptional activation. *Cell Rep.* **12**, 622–635 (2015).
46. Brown, R. D. et al. Prognostically significant cytotoxic T cell clones are stimulated after thalidomide therapy in patients with multiple myeloma. *Leuk. Lymphoma* **50**, 1860–1864 (2009).
47. Raitakari, M. et al. T-cell expansions in patients with multiple myeloma have a phenotype of cytotoxic T cells. *Br. J. Haematol.* **110**, 203–209 (2000).
48. Tienhaara, A. & Pelliniemi, T. T. Peripheral blood lymphocyte subsets in multiple myeloma and monoclonal gammopathy of undetermined significance. *Clin. Lab. Haematol.* **16**, 213–223 (1994).
49. Wu, L. et al. Lenalidomide enhances antibody-dependent cellular cytotoxicity of solid tumor cells in vitro: influence of host immune and tumor markers. *Cancer Immunol. Immunother.* **60**, 61–73 (2011).
50. Jurisic, V., Srdic, T., Konjevic, G., Markovic, O. & Colovic, M. Clinical stage-depending decrease of NK cell activity in multiple myeloma patients. *Med. Oncol.* **24**, 312–317 (2007).
51. Ponzetta, A. et al. Multiple myeloma impairs bone marrow localization of effector natural killer cells by altering the chemokine microenvironment. *Cancer Res.* **75**, 4766–4777 (2015).
52. Zelle-Rieser, C. et al. T cells in multiple myeloma display features of exhaustion and senescence at the tumor site. *J. Hematol. Oncol.* **9**, 116 (2016).
53. Castella, B., Foglietta, M., Riganti, C. & Massaia, M. V γ V δ 2 T Cells in the bone marrow of myeloma patients: a paradigm of microenvironment-induced immune suppression. *Front. Immunol.* **9**, 1492 (2018).
54. Chan, A. C. et al. Natural killer T cell defects in multiple myeloma and the impact of lenalidomide therapy. *Clin. Exp. Immunol.* **175**, 49–58 (2014).
55. Dhodapkar, M. V. & Richter, J. Harnessing natural killer T (NKT) cells in human myeloma: progress and challenges. *Clin. Immunol.* **140**, 160–166 (2011).
56. Castella, B., Melaccio, A., Foglietta, M., Riganti, C. & Massaia, M. V γ V δ 2 T cells as strategic weapons to improve the potency of immune checkpoint blockade and immune interventions in human myeloma. *Front. Oncol.* **8**, 508 (2018).
57. Ortiz, M. L., Lu, L., Ramachandran, I. & Gabrilovich, D. I. Myeloid-derived suppressor cells in the development of lung cancer. *Cancer Immunol. Res.* **2**, 50–58 (2014).
58. Fang, Z. et al. Myeloid-derived suppressor cell and macrophage exert distinct angiogenic and immunosuppressive effects in breast cancer. *Oncotarget* **8**, 54173–54186 (2017).
59. Gabrilovich, D. I., Ostrand-Rosenberg, S. & Bronte, V. Coordinated regulation of myeloid cells by tumours. *Nat. Rev. Immunol.* **12**, 253–268 (2012).
60. Quail, D. F. F. & Joyce, J. A. Microenvironmental regulation of tumor progression and metastasis. *Nat. Med.* **19**, 1423–1437 (2013).
61. Zheng, G. X. et al. Massively parallel digital transcriptional profiling of single cells. *Nat. Commun.* **8**, 14049 (2017).
62. Taylor-Weiner, A. et al. Scaling computational genomics to millions of individuals with GPUs. *Genome Biol.* **20**, 228 (2019).
63. Tan, V. Y. F. & Févotte, C. Automatic relevance determination in nonnegative matrix factorization with the β -divergence. *IEEE Trans. Pattern Anal. Mach. Intell.* **35**, 1592–1605 (2013).

Acknowledgements

We thank the Dana-Farber/Harvard Cancer Center in Boston for the use of the Specialized Histopathology Core for histology and immunohistochemistry service. The Dana-Farber/Harvard Cancer Center is supported in part by a National Cancer Institute Cancer Center Support Grant no. NIH 5 P30 CA06516. G.G. was partially funded by the Paul C. Zamecnik Chair in Oncology, Massachusetts General Hospital Cancer Center. N.J.H. was partially funded by G.G. startup funds at Massachusetts General Hospital, R01 (principal investigator I.M.G.) and the Harvard Graduate Program in Biophysics, Harvard University. Molecular Biophysics Training Grant NIH/NIGMS T32 GM008313 (N.J.H.; principal investigator J. M. Hogle). This study was partially funded by two National Institutes of Health grants (no. NIH R01 CA 205954 and R01CA181683), the Leukemia and Lymphoma Society, the Multiple Myeloma Research Foundation and Stand Up to Cancer.

Author contributions

O.Z., T.H.M., I.M.G., N.J.H. and G.G. conceived and designed the study. T.H.M. collected patient data and performed cytogenetic analyses. O.Z. generated the single-cell sequencing and CyTOF data, and performed in vivo experiments. O.Z. and T.H.M. performed in vitro experiments. N.J.H. processed and analyzed the single-cell sequencing data. O.Z. and N.J.H. integrated and interpreted the data. M.G., M.C., J.L.G. and S.A.M. assisted in setup of the study. J.P., M.X.H., C.-J.L., Y.E.M. and E.M.V.A. performed preliminary analyses. N.K.S., D.H. and B.B. managed clinical samples. R.F., E.B., B.F., A.F., S.C., M.P.A., M. Reidy, M. Rahmat, S.M. and M.B. performed validation experiments. I.M.G., G.G. and J.A. supervised the study. O.Z., N.J.H., T.H.M., R.S.P., G.G. and I.M.G. wrote the manuscript.

Competing interests

G.G. receives research funds from IBM and Pharmacyclics and is an inventor on patent applications related to MuTect, ABSOLUTE, MutSig, MSMuTect and

POLYSOLVER. I.M.G. has a consulting/advisory role with GSK, AbbVie and Bristol Myers Squibb. I.M.G has a consulting role with Sanofi, Janssen Pharmaceuticals, Takeda, Celgene, Karyopharm, GNS, Celllectar Biosciences, Medscape, Genetech, Adaptive Biotechnologies, Aptitude, Curio Science, Magenta Therapeutics and Oncopeptides. I.M.G. received research funding/ honoraria from Celgene, Takeda, Bristol Myers Squibb, Janssen Pharmaceuticals and Amgen.

Additional information

Extended data is available for this paper at <https://doi.org/10.1038/s43018-020-0053-3>.

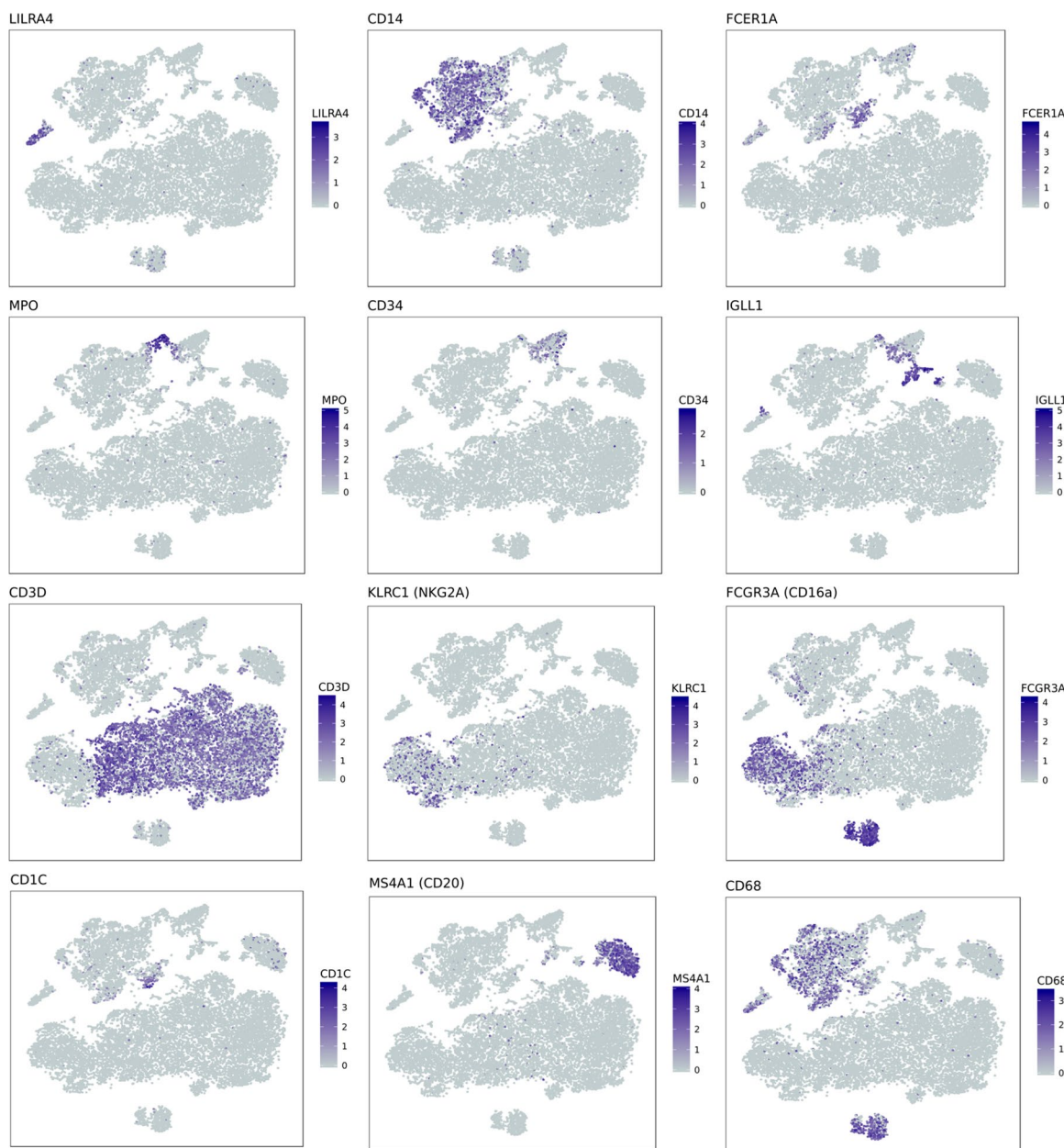
Supplementary information is available for this paper at <https://doi.org/10.1038/s43018-020-0053-3>.

Correspondence and requests for materials should be addressed to G.G. or I.M.G.

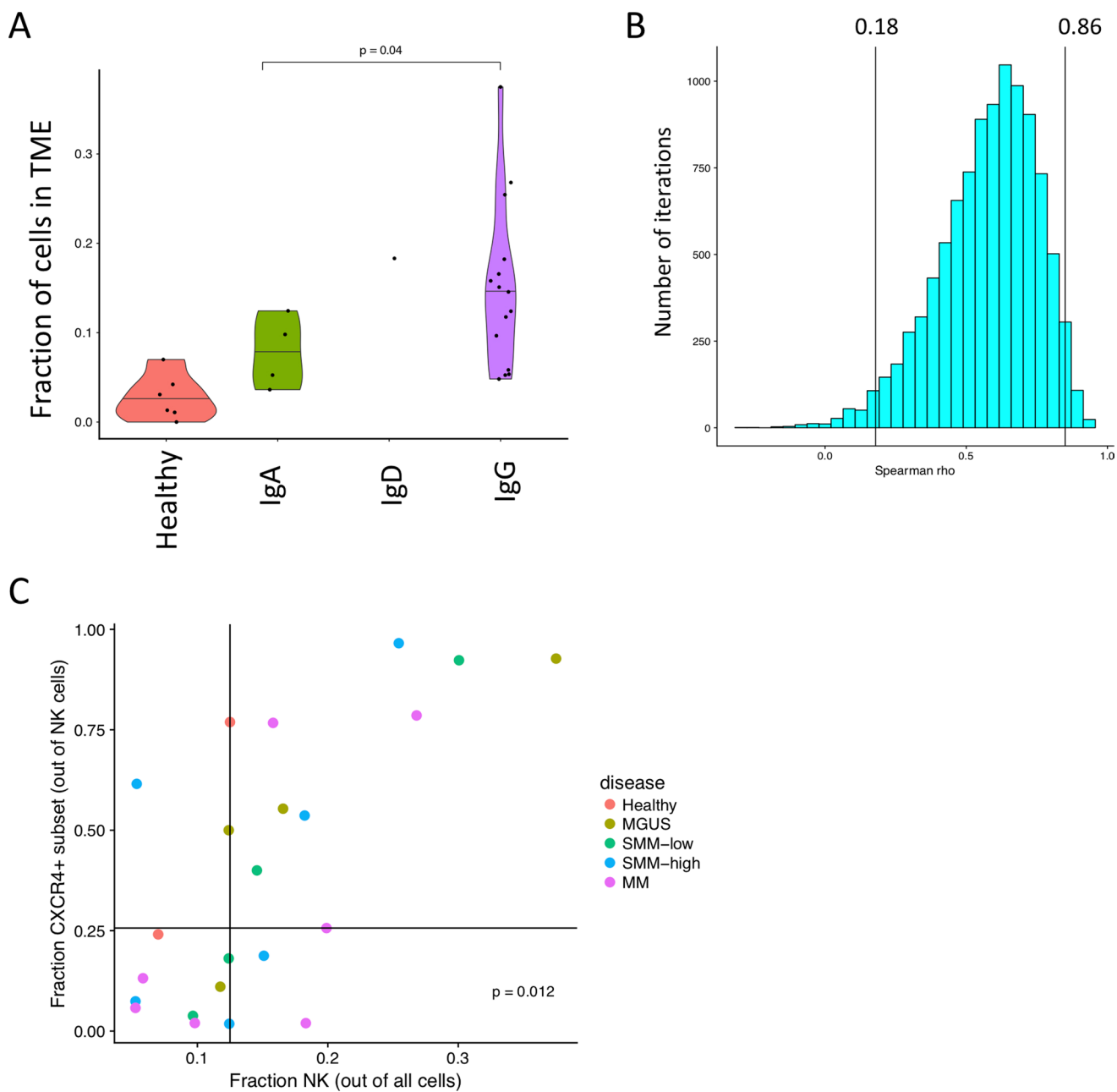
Reprints and permissions information is available at www.nature.com/reprints.

Publisher's note Springer Nature remains neutral with regard to jurisdictional claims in published maps and institutional affiliations.

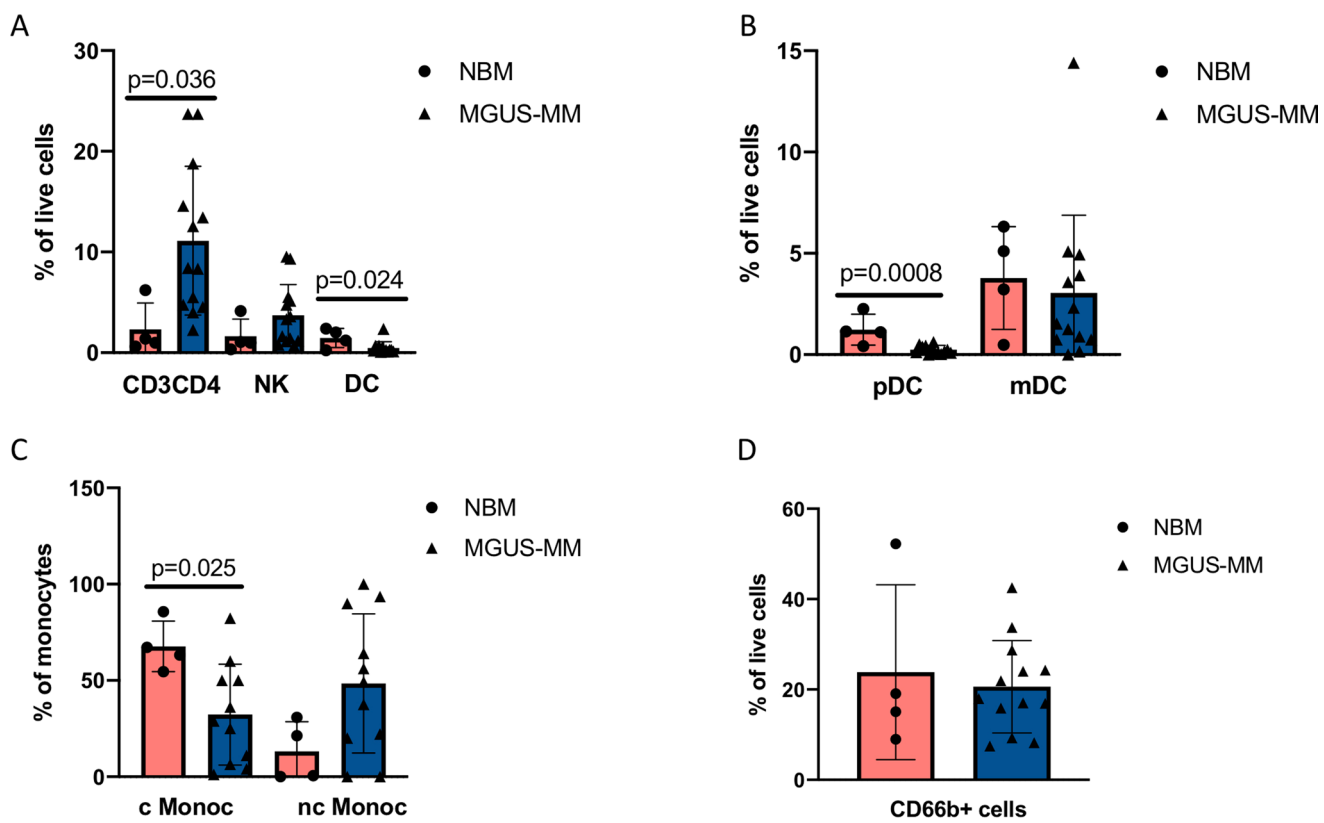
© The Author(s), under exclusive licence to Springer Nature America, Inc. 2020



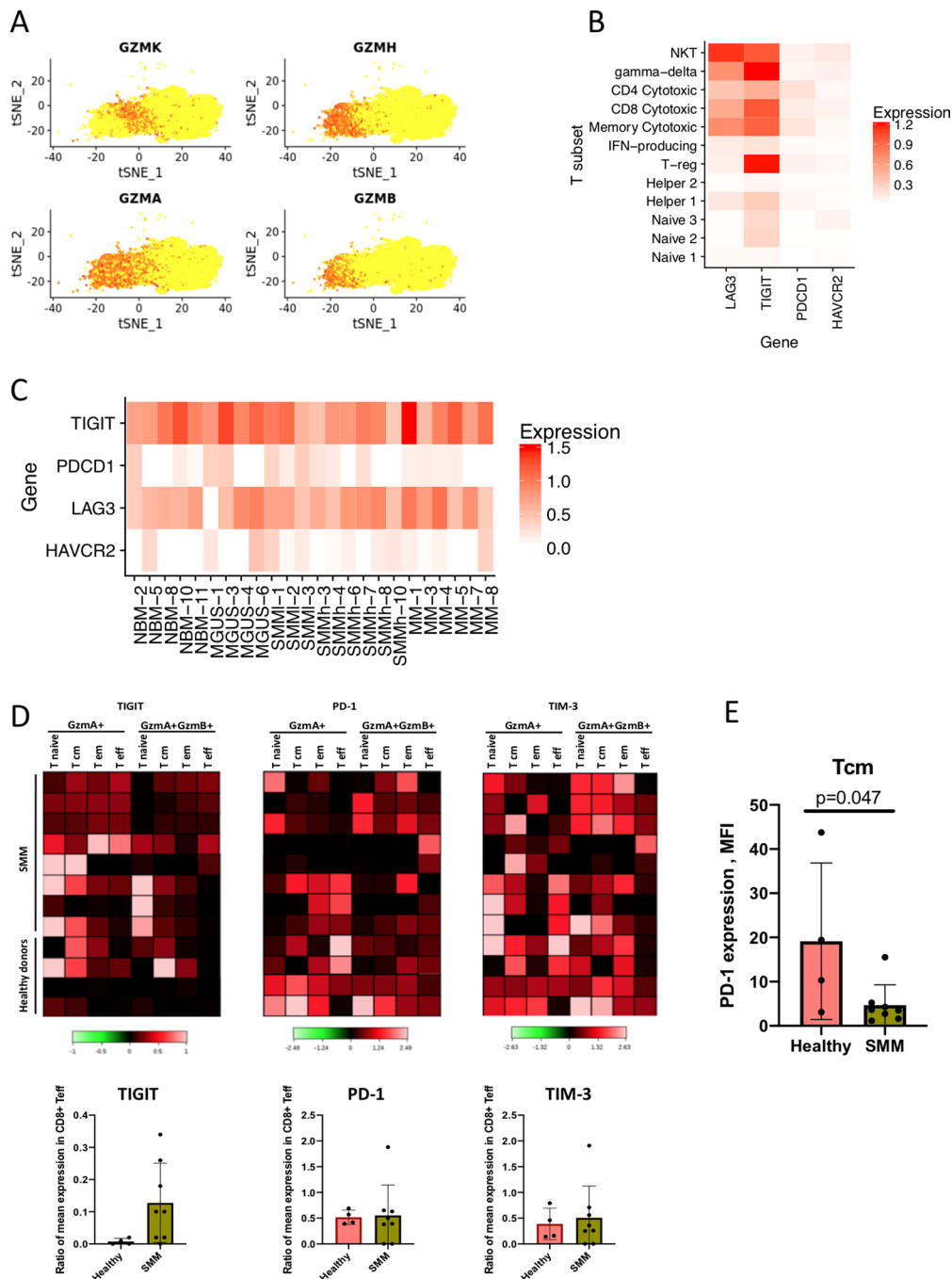
Extended Data Fig. 1 | Marker genes demonstrating cell type identity of immune cell clusters. tSNE representation of CD45 cell populations. In each subplot, cells are colored by log-normalized expression values for a given cell type specific marker gene.



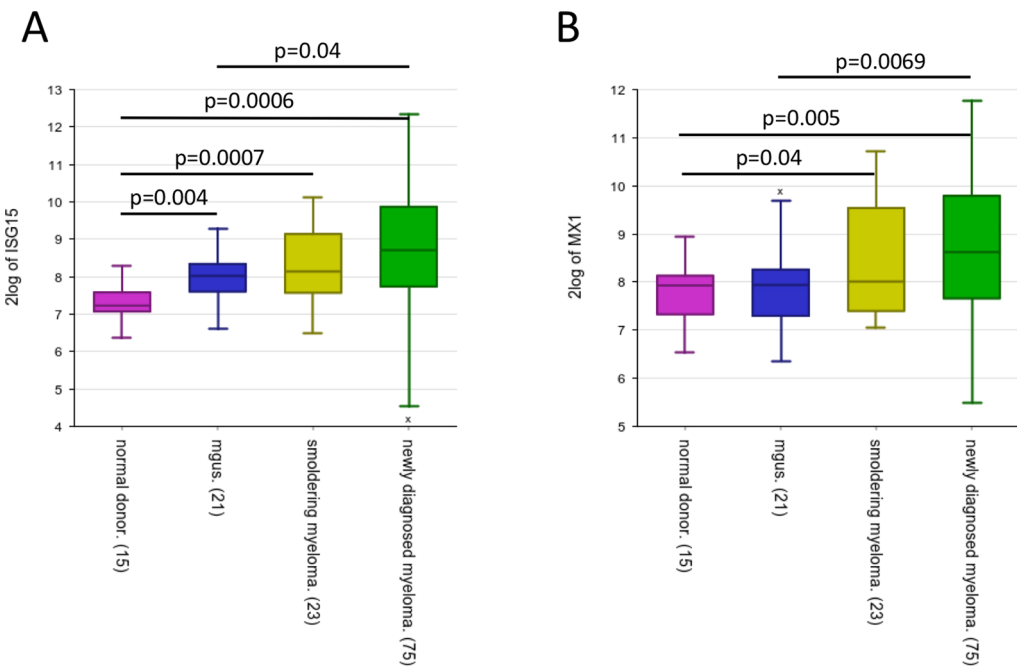
Extended Data Fig. 2 | Single-cell RNA sequencing results indicate changes in NK cell compartment as compared to healthy donors. **a**, A significant increase in the fraction of NK cells in patients with malignant cells expressing IgG heavy chain. Fractions of NK cells are plotted for patients grouped by immunoglobulin heavy chain. Violin plots show minimum, median, and maximum values. A two-tailed t-test was performed on $n=19$ patient samples with $df=12$. **b**, Spearman correlation between NK cell fraction and CXCR4⁺ subset frequency calculated on 10,000 samples with replacement of data points. 95% confidence interval is shown. **c**, Grouping of samples above and below median values for NK cell frequencies and CXCR4⁺ subset fractions. Points on the median were assigned in the conservative direction (that is to obtain a less significant p-value). A two-sided fisher-exact test was performed on $n=23$ patient samples.



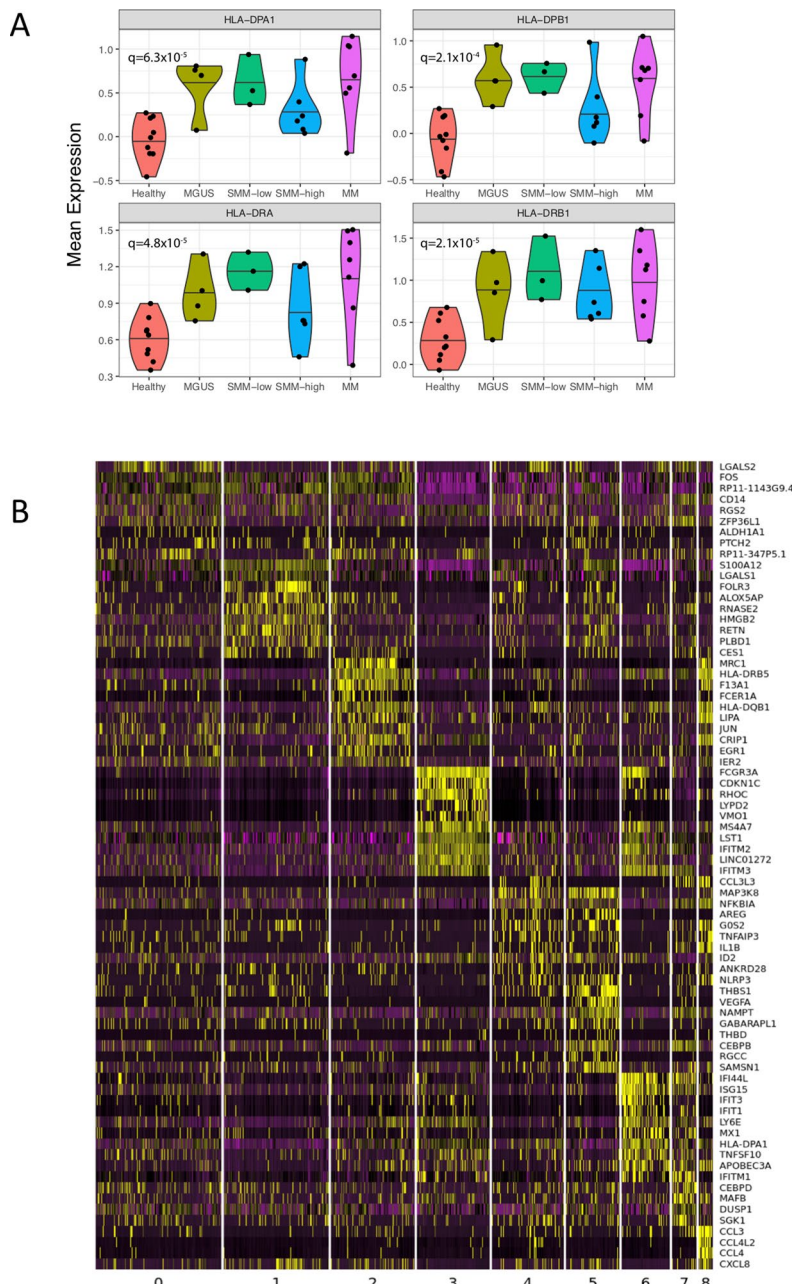
Extended Data Fig. 3 | Compositional alterations in immune populations of diseased patients as compared to healthy donors. CyTOF profiling of 4 healthy donors and 13 MGUS-MM patients show **a**, significantly increased numbers of CD3⁺CD4⁺ T cells in BM aspirates of the patients as compared to healthy BM with mean values of 2.3 and 11.12 for CD3⁺CD4⁺, 1.6 and 3.7 for NK, and 1.5 and 0.5 for dendritic cells (DC) in healthy donors and MM patients respectively. Significant difference between groups was tested using a two-sided t-test. Bars represent SD. **b**, Plasmacytoid DC (pDC) are significantly enriched in healthy BM as compared to MM patients with mean values of 1.2 and 0.26 respectively. Mean values for monocytic DC (mDC) are 3.7 and 3.2 for healthy donors and MM patients respectively. Significant difference between groups was tested using a two-sided t-test. Bars represent average deviation. **c**, Classical monocytes (c Monoc) are enriched in BM aspirates of healthy donors compared to MM patients with respective mean values of 67.7 and 26.5. Mean values for non-classical monocytes (nc Monoc) were 13.1 and 44.4 for healthy donors and MM patients respectively. Significant difference between groups was tested using a two-sided t-test. Bars represent average deviation. **d**, Proportion of CD66b⁺ cells in BM aspirates of SMM patients and healthy donors. Mean values are 23.8 and 20.6 for healthy donors and MM patients respectively. Significant difference between groups was tested using a two-sided t-test. Bars represent SD.



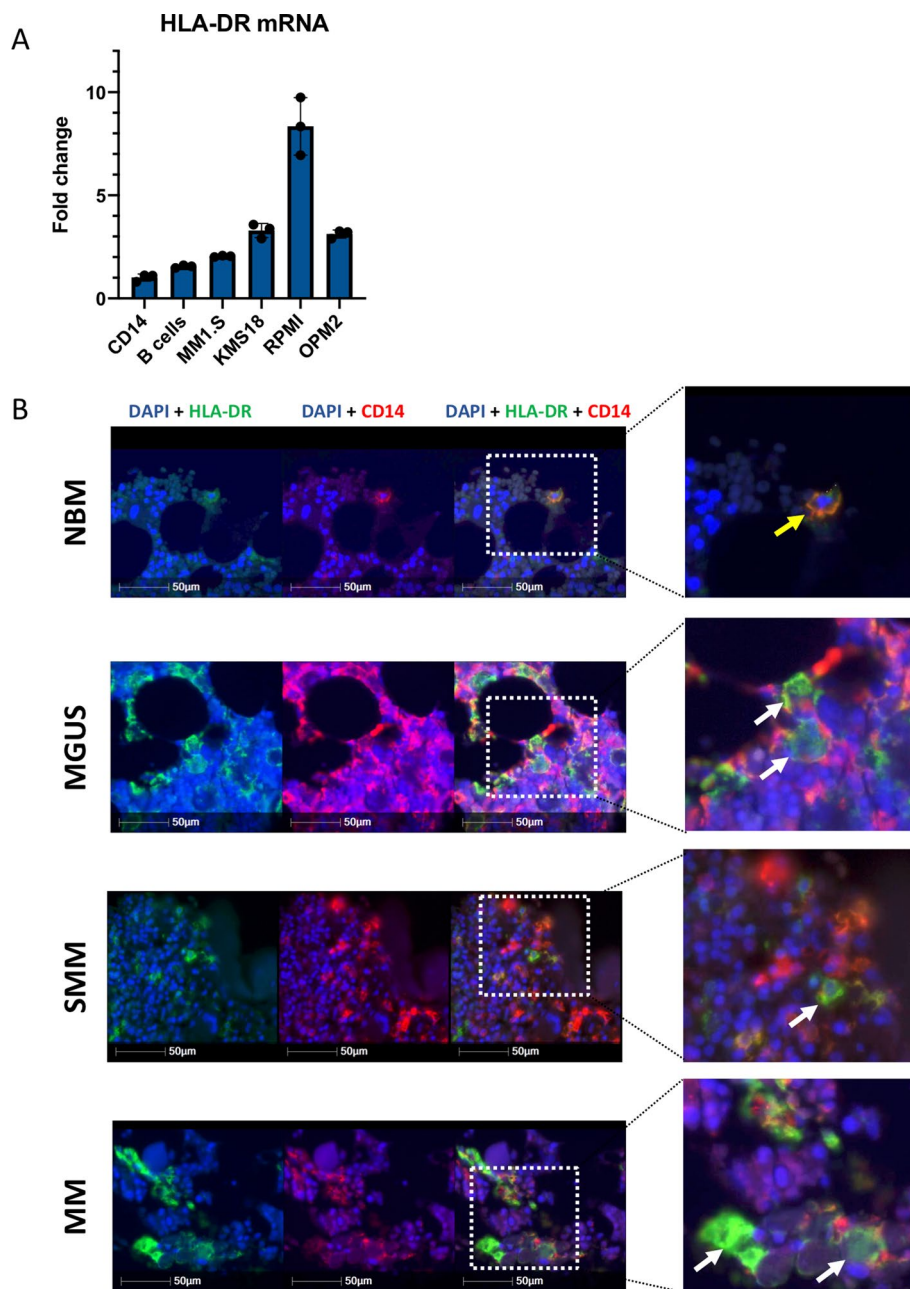
Extended Data Fig. 4 | Transcriptional alterations in cytotoxic T cell populations of diseased patients as compared to healthy donors. **a**, Distribution of the Granzyme expression in T-cell cluster. GZMA⁺GZMB⁻ corresponds to the *Granzyme K* expressing cells. **b**, Normalized expression values for four exhaustion-related genes across different T cell subsets, pooling cells across patients. **c**, Normalized expression values for four exhaustion-related genes across different donors and patients, pooling cells across T subsets. **d**, Heatmap of immune checkpoint molecules expression levels on different subsets of bone marrow T cells in SMM patients (n=8) as compared to healthy donors (n=4). Individual patients show increased levels of PD-1 and TIGIT in GrB expressing effector cells. Colored scale represents transformed ratio of protein expression. Barplots show variable expression of TIGIT (with mean values of 0.01 vs 0.12), PD-1 (0.52 vs. 0.55) and TIM-3 (0.39 vs. 0.51) in GrB-expressing T effectors from healthy BM and SMM patients respectively. Significant difference between groups was tested using a two-sided t-test. Bars represent SD. **e**, Healthy memory cells show significantly higher expression of PD-1 compared to those of SMM patients with mean values of 19.5 and 4.7 respectively. Significant difference between groups was tested using a two-sided t-test. Bars represent SD.



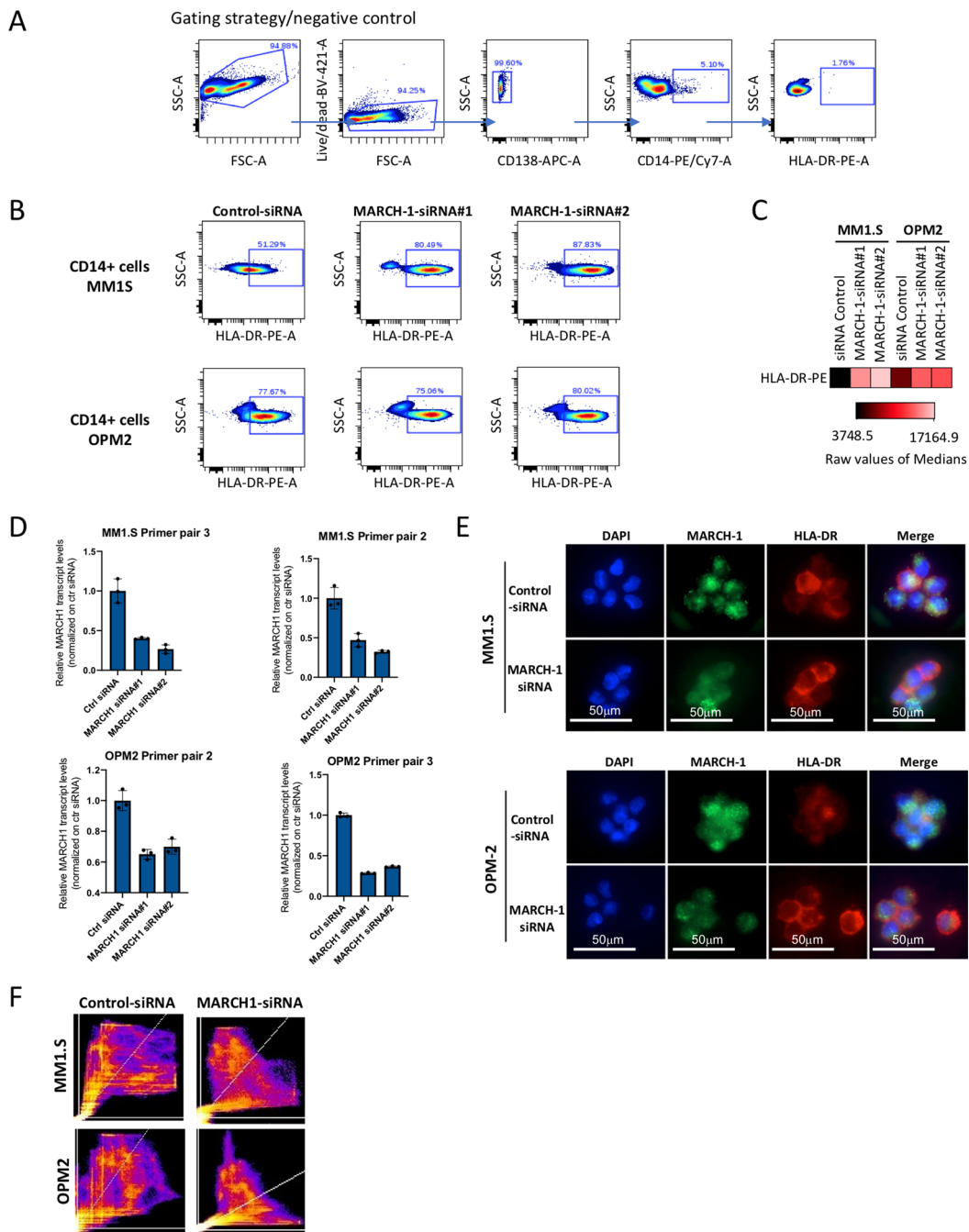
Extended Data Fig. 5 | IFN type-1 signaling increases in plasma cells during disease progression. Expression of *ISG15* **a**, and *MX1* **b**, increases during disease progression. Significant difference is observed between MGUS and MM stage, indicating an increase of IFN signals at later stages in the disease progression (GSE6477). Box plot displays the first quartile, median and third quartile for the gene expression levels, bars indicate the minimum and maximum value. Significant difference between groups was tested using one-way ANOVA and Tukey multiple comparison tests for healthy donors (ND, n=15), MGUS (n=21), SMM (n=23) and newly diagnosed MM (n=75).



Extended Data Fig. 6 | Marker genes demonstrating cell type identity of monocytic clusters. **a**, Mean expression of MHC II encoding genes. Violin plots show minimum, median, and maximum values. A BH-corrected two-tailed t-test was performed on n=32 patient samples. **b**, Heatmap of expression values for the top 10 genes with enriched expression in all monocytes discovered by k-nearest neighbors' subclustering. Expression values are centered and normalized for each gene.

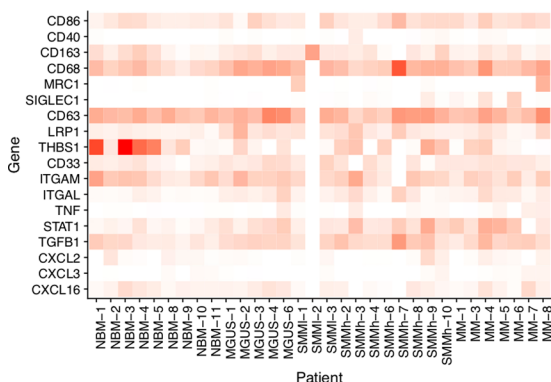


Extended Data Fig. 7 | Dysregulation of HLA-DR surface representation in monocytes from diseased environment. **a**, qPCR data demonstrate significant increase of HLA-DR expression in CD14⁺ monocytes after co-culture with MM cell lines. CD14⁺ cells alone and those co-cultured with B cells were used as a control. Median ratios were 1.54 for B cells, 2.07 for MM1.S cells, 3.28 for KMS-18, 8.34 for RPMI and 3.12 for OPM2 cells as compared to CD14⁺ control (1.0). Bars represent SD. Experiment was performed twice with independent donors in triplicates. Representative data from one experiment is shown. **b**, Immunofluorescence staining of tissue microarrays from MGUS, SMM and MM patients (n=45, TMA performed in triplicates, total of 135 BM sections analysed) demonstrates prevalent intracellular accumulation of HLA-DR (green) in CD14-expressing monocytes (red) in disease settings. Membrane-bound localization of HLA-DR was observed in healthy bone marrow monocytes. (yellow arrows point on cells with HLA-DR localized to the cell membrane, white arrows point on cells with HLA-DR accumulated in the cytoplasm).

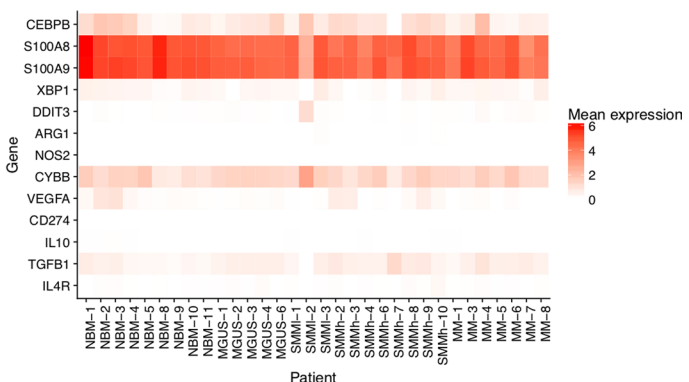


Extended Data Fig. 8 | MARCH-1 dependent internalization of HLA-DR in CD14⁺ monocytes in myeloma environment. **a**, Gating strategy for HLA-DR on CD14⁺ cells. **b**, Knockdown of MARCH-1 by siRNA rescues presentation of HLA-DR molecules on the surface of CD14⁺ monocytes co-cultured with MM cells. Representative FACS profiles show higher numbers of HLA-DR⁺ cells after MARCH-1 knockdown with siRNA (experiment performed 3 times with 3 different donors using 2 different cell lines/2 different siRNAs for MARCH-1, non-targeting si-RNA is used as a control). **c**, Mean fluorescence intensity demonstrates the two to 4.5-fold increase in the levels of HLA-DR protein expression on the cell surface of CD14⁺ cells. **d**, qPCR data for relative expression of MARCH-1 in CD14⁺ cells after siRNA knockdown as compared to the si-RNA control. The assay was performed twice with independent donors/2 cell lines/2 siRNAs, performed in triplicates. Representative data from one experiment is shown. In MM1.S cells, siRNA knockdown leads to reduction of MARCH-1 expression to 0.46 and 0.32 (median value, amplified with primer pair 2) and to 0.40 and 0.26 (median value, amplified with primer pair 3) as compared to control siRNA (median value, 1.0). In OPM2 cells, siRNA knockdown leads to reduction of MARCH-1 expression to 0.65 and 0.7 (median value, amplified with primer pair 2) and to 0.29 and 0.36 (median value, amplified with primer pair 3) as compared to control siRNA (median value, 1.0). Bars represent STDEV. **e**, CD14⁺ cells with lower levels of MARCH-1 have increased HLA-DR protein on their cell surface. The experiment was performed twice with two independent donors/2 cell lines/2 siRNAs. **f**, Stronger correlation of DAPI and HLA-DR localization in MM1.S and OPM2 cells in control cells as compared to those after MARCH-1-siRNA transfection. The experiment was performed twice with two independent donors/2 cell lines/2 siRNAs.

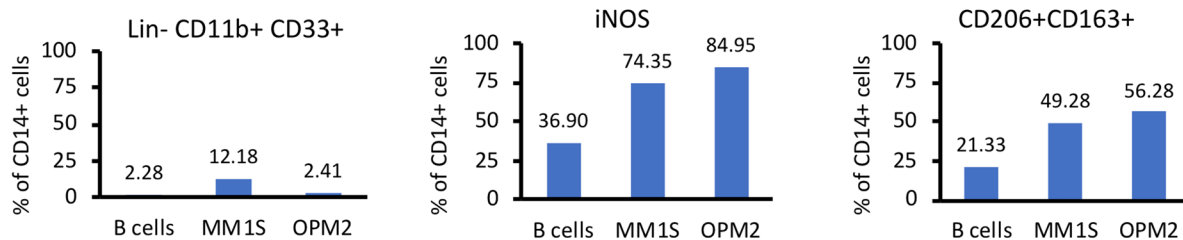
A



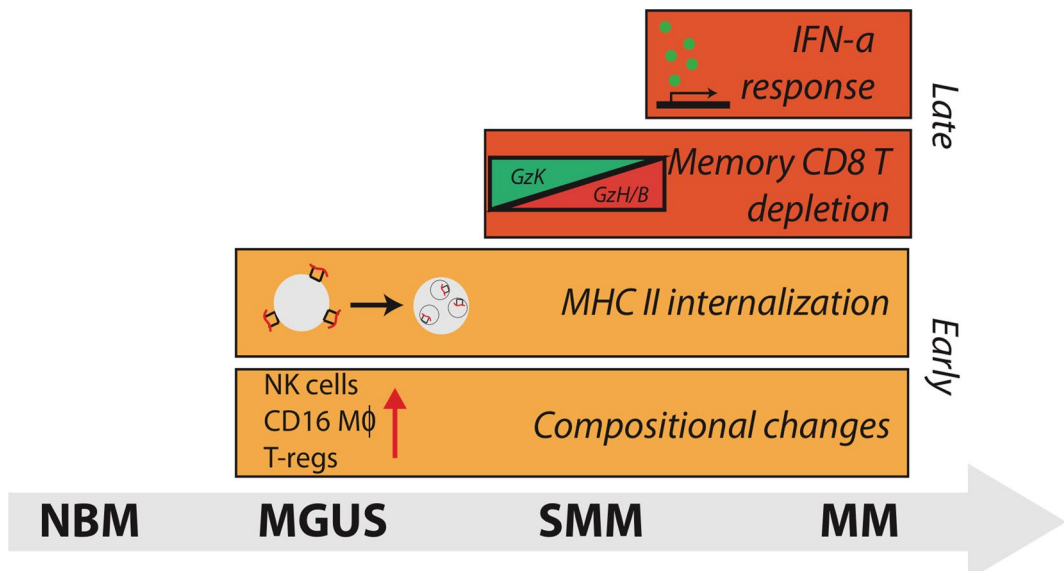
B



C



Extended Data Fig. 9 | CD14⁺ monocytes do not show the M-MDSC phenotype after co-culture with MM cells. Expression of different markers for **a**, macrophages/monocytes and **b**, MDSCs on CD14⁺ cells in patients and healthy donors. **c**, CD14⁺ cells from healthy donors were co-cultured with MM cells. FACS analysis was performed on day 3 after co-culture. Representative results from one out of two independent experiments performed with two healthy donors/2 different cell lines. Due to restricted cell numbers, no replicates could be used. All donors have similar distribution of cells as compared to controls.



Extended Data Fig. 10 | Alterations in tumor microenvironment start from the precursor stages of the MM and exhibit heterogeneous changes in the immune cell repertoire. Illustration of immune alterations observed during progression. Bars begin at the stage in which they are first observed in our dataset.

Reporting Summary

Nature Research wishes to improve the reproducibility of the work that we publish. This form provides structure for consistency and transparency in reporting. For further information on Nature Research policies, see [Authors & Referees](#) and the [Editorial Policy Checklist](#).

Statistics

For all statistical analyses, confirm that the following items are present in the figure legend, table legend, main text, or Methods section.

n/a Confirmed

- The exact sample size (n) for each experimental group/condition, given as a discrete number and unit of measurement
- A statement on whether measurements were taken from distinct samples or whether the same sample was measured repeatedly
- The statistical test(s) used AND whether they are one- or two-sided
Only common tests should be described solely by name; describe more complex techniques in the Methods section.
- A description of all covariates tested
- A description of any assumptions or corrections, such as tests of normality and adjustment for multiple comparisons
- A full description of the statistical parameters including central tendency (e.g. means) or other basic estimates (e.g. regression coefficient) AND variation (e.g. standard deviation) or associated estimates of uncertainty (e.g. confidence intervals)
- For null hypothesis testing, the test statistic (e.g. F , t , r) with confidence intervals, effect sizes, degrees of freedom and P value noted
Give P values as exact values whenever suitable.
- For Bayesian analysis, information on the choice of priors and Markov chain Monte Carlo settings
- For hierarchical and complex designs, identification of the appropriate level for tests and full reporting of outcomes
- Estimates of effect sizes (e.g. Cohen's d , Pearson's r), indicating how they were calculated

Our web collection on [statistics for biologists](#) contains articles on many of the points above.

Software and code

Policy information about [availability of computer code](#)

Data collection

Single Cell RNA sequencing using 10xGenomics v2, Illumina HiSeq 2500/4000 sequencing platforms demultiplexing and alignment of scRNA sequencing data was performed with Cell Ranger-Single cell software Suite v2.0.1 (10x Genomics, open source)

Data analysis

Enrichment scores for genes were established using Seurat v2.3.1
Cell clusters were identified using Seurat v2.3.1 KNN clustering
NMF-derived gene expression signatures were identified using SignatureAnalyzer-GPU (<https://github.com/broadinstitute/SigntureAnalyzer-GPU>)
CyTOF data were analyzed using automated analysis GemStone software (Verity) for events purification and analyzed in Cytobank premium

For manuscripts utilizing custom algorithms or software that are central to the research but not yet described in published literature, software must be made available to editors/reviewers. We strongly encourage code deposition in a community repository (e.g. GitHub). See the Nature Research [guidelines for submitting code & software](#) for further information.

Data

Policy information about [availability of data](#)

All manuscripts must include a [data availability statement](#). This statement should provide the following information, where applicable:

- Accession codes, unique identifiers, or web links for publicly available datasets
- A list of figures that have associated raw data
- A description of any restrictions on data availability

Gene expression data can be accessed at GSE124310 and DbGap repository (phs001323.v1.p1)

Field-specific reporting

Please select the one below that is the best fit for your research. If you are not sure, read the appropriate sections before making your selection.

Life sciences

Behavioural & social sciences

Ecological, evolutionary & environmental sciences

For a reference copy of the document with all sections, see nature.com/documents/nr-reporting-summary-flat.pdf

Life sciences study design

All studies must disclose on these points even when the disclosure is negative.

Sample size

No statistical methods were used to predetermine samples sizes. Available clinical samples with sufficient numbers of cells were used. The sample size was sufficient to detect statistically significant compositional and expression changes between case and controls after multiple hypothesis correction.

Data exclusions

- Cells called by Cell Ranger v2.0.1 were filtered to those with <10% mitochondrial expression, >200 genes covered, and >600 total UMLs to remove low quality cells.
- We excluded ultra-highly expressed genes that were drastically higher in expression for the other compartment (eg. IgGs from plasma cells, HBB, HBA2) to remove confounding effects of cross-cell contamination present in highly expressed genes.
- We excluded samples in which low (<50) cells were detected since these cases could not provide accurate measurements of relative cell frequencies or gene expression.

These exclusion metrics were based on the distribution of the data, and could not be pre-determined.

Replication

All attempts for replications were successful

- for validation analyses, experiments were repeated at least 2 times using at least 2 different donors and at least 2 different MM cell lines
- for siRNA silencing experiments 2 different siRNAs were used, experiment repeated 3 times
- for T cell profiling CyTOF experiments data were pooled from 2 independent runs

Randomization

Our study of patient data is observational, and thus randomization is not used.

Blinding

-blinding was not possible for bioinformatic analyses, but unsupervised clustering method was used

Reporting for specific materials, systems and methods

We require information from authors about some types of materials, experimental systems and methods used in many studies. Here, indicate whether each material, system or method listed is relevant to your study. If you are not sure if a list item applies to your research, read the appropriate section before selecting a response.

Materials & experimental systems

n/a	Involved in the study
<input type="checkbox"/>	<input checked="" type="checkbox"/> Antibodies
<input type="checkbox"/>	<input checked="" type="checkbox"/> Eukaryotic cell lines
<input checked="" type="checkbox"/>	<input type="checkbox"/> Palaeontology
<input type="checkbox"/>	<input checked="" type="checkbox"/> Animals and other organisms
<input type="checkbox"/>	<input checked="" type="checkbox"/> Human research participants
<input type="checkbox"/>	<input checked="" type="checkbox"/> Clinical data

Methods

n/a	Involved in the study
<input checked="" type="checkbox"/>	<input type="checkbox"/> ChIP-seq
<input type="checkbox"/>	<input checked="" type="checkbox"/> Flow cytometry
<input checked="" type="checkbox"/>	<input type="checkbox"/> MRI-based neuroimaging

Antibodies

Antibodies used

-CyTOF: Maxpar® Human Immune Monitoring Panel Kit, 29-marker panel, Fluidigm, Catalog number: 201324, dilution 1:100 for 1-3 Mio of cells
 PD1-175Lu (clone EH12.2H7, PRODUCT # 3175008B, Fluidigm, 1:100), TIM3-153Eu (clone F38-2E2, PRODUCT # 3153008B, Fluidigm, 1:100), Granzyme B-171Yb (clone GB11, PRODUCT # 3171002B, Fluidigm, 1:100), TIGIT-143Nd (clone MBSA43, Fisher Scientific, cat number 50-147-83, 1:100) and Granzyme A (clone CB9, BioLegend, cat. number 507202, 1:50)-conjugated with 143 Nd (PRODUCT # 201143A, Maxpar Fluidigm) and 149Sm (PRODUCT # 201149A, Maxpar Fluidigm) respectively and Maxpar® Human T- Cell Phenotyping Panel Kit, 16 Marker, Catalog number: 201305, dilution 1:100 for 1-3 Mio of cells
 -Flow Cytometry: Anti-human antibodies against CD138 (clone MI15, BioLegend, cat number 356505, 1:20), CD14 (clone 63D3, BioLegend, cat number 367111, 1:20), HLA-DR (clone L243, BioLegend, cat number 307609, 1:20), HLA-DP (DP11.1, Santa Cruz Biotechnologies, cat number SC-53308 FITC, 1:50), INOS (clone SP126, Abcam, cat number ab115819, 1:100), CD33 (clone WM53, BioLegend, cat number 303413, 1:20), CD11b (clone ICRF44, BioLegend, cat number 301341, 1:20), CD206 (clone 15-2, BioLegend, cat number 321113, 1:20), CD163 (clone GHI/61, BioLegend, cat number 333621, 1:20) and FITC anti-human Lineage Cocktail (UCHT1, HCD14, 3G8, HIB19, 2H7, HCD56, BioLegend, cat number 348801, 1:5), PerCP/Cy5.5 anti-human CD4 (BioLegend, 317428, clone OKT4, 1:20); BV510 anti-human CD44 (Biolegend, 103044, clone IM7, 1:20); APC/Cy7 anti-human CD8 (BioLegend, 300926, clone HIT8a, 1:20)

-Cell selection: Human CD138+ plasma cells, CD45+ immune cells, CD14+ monocytes or CD19+ B-cells were obtained from fresh BM/PB cells using CD138 (130-051-301, Miltenyi Biotec), CD45 (130-045-801, Miltenyi Biotec), CD14 (130-050-201, Miltenyi Biotec) and CD19 (130-050-301, Miltenyi Biotec) MicroBeads (clone info not available).
 -Dual-Immunohistochemistry staining was performed using anti-CD14 (1:100; clone D7A2T, Cell Signaling Technologies, cat number 75181) that is detected by Alexa FluorTM 594 Tyramide Reagent from Life Technologies catalogue #B40957, and anti-HLA-DR (1:500; clone TAL.1B5, Dako) detected by Alexa FluorTM 488 Tyramide Reagent from Life Technologies catalogue # B40953, 1:100)
 -Cytospins: MARCH-1 (polyclonal rabbit anti-human, Life Technologies, PA553199, 1:100) and HLA-DR (clone L243, mouse anti-human, BioLegend, 307602, 1:100), goat-anti-mouse-Alexa Fluor 594 (Fisher Scientific, A-11032, 1:100), goat-anti-rabbit Alexa Fluor 488 (abcam, ab-92511, 1:100)

Validation

All antibodies used were commercially available. Information about antibody validation from BioLegend can be found here: <https://www.biologend.com/en-us/quality-control>.
 Information about validation of Maxpar® Human Immune Monitoring Panel is here: <https://www.fluidigm.com/binaries/content/documents/fluidigm/search/hippo%3Aresultset/maxpar-him-white-paper-2018/fluidigm%3Afile>
 Cell Signaling Technologies: https://www.cellsignal.com/contents/_cst-antibody-validation-principles/ourapproach-validation-principles
 Abcam: <https://www.abcam.com/primary-antibodies/how-we-validate-our-antibodies>
 Fisher scientific: <https://www.thermofisher.com/us/en/home/life-science/antibodies/invitrogen-antibody-validation.html?cid=ab-search-learning-ab-validation>

Eukaryotic cell lines

Policy information about [cell lines](#)

Cell line source(s)	Human MM.1S and RPMI-8226 cells were purchased from ATCC, KMS-18 myeloma cell line was obtained from the Japanese Collection of Research Bioresources (JCRB), Japan. OPM2 cells were obtained from DSMZ.
Authentication	All cell lines were authenticated with STR fingerprinting at the Michigan State University Genomics core
Mycoplasma contamination	All cell lines were negative for mycoplasma contamination
Commonly misidentified lines (See ICLAC register)	none of the cell lines used are listed in the ICLAC database

Animals and other organisms

Policy information about [studies involving animals; ARRIVE guidelines](#) recommended for reporting animal research

Laboratory animals	Mus musculus, C57BL/6J mice were purchased from Jackson Laboratories (Stock No: 000664, Bar Harbor, Maine). C57BL/KaLwRijHsd mice were purchased from Envigo (Netherlands). In experimental settings female and male mice in the age of 10 weeks, 6 months or 1,5 years were used.
Wild animals	the study did not involve wild animals.
Field-collected samples	the study did not involve samples collected from the field.
Ethics oversight	All mice were treated, monitored, and sacrificed in accordance with an approved protocol of the Dana-Farber Cancer Institute Animal Care and Use Committee.

Note that full information on the approval of the study protocol must also be provided in the manuscript.

Human research participants

Policy information about [studies involving human research participants](#)

Population characteristics	newly diagnosed, untreated multiple myeloma, MGUS and Smoldering myeloma patients (IRB 14-174, 07-150). Male and female patients in the average age of 64+-8.8 (average +/- STDEV). Participants were recruited to the tissue banking protocols 14-174 and 07-150 based on having a diagnosis of MGUS, Smoldering myeloma or myeloma and being interested in donating a research bone marrow or peripheral blood sample to DFCI.
Recruitment	Participants were recruited to the tissue banking protocols 14-174 and 07-150 based on having a diagnosis of MGUS, Smoldering myeloma or myeloma and being interested in donating a research bone marrow or peripheral blood sample to DFCI. New patients eligible for precursor tissue banking or their legal guardians were consented by clinical research personnel during standard-of-care visits or received enrollment information via postal mail or through secure electronic transmission. Publicity of the project occurred online via Internet advertising through patient-targeted websites and social media sites including but not limited to the Leukemia and Lymphoma Society, the Multiple Myeloma Research Foundation (MMRF), Facebook, Twitter, and the MPN Research Foundation websites among others. This approach to recruitment resulted in a large portion of the cohort coming from patients apt to select to receive care from DFCI. There is also the possibility that this cohort is composed of patients with greater access and comfort using the computer and the Internet. However, for the present study, only samples from participants diagnosed and undergoing bone marrow aspiration at DFCI were used. Access to the database is double password-

protected and HIPPA compliant with links between the multiple tables tied to the coded research laboratory number assigned to each patient.

Ethics oversight

Human studies were approved by the Dana-Farber Cancer Institute Institutional Review Board (Boston, USA). Informed consent was obtained from all patients and healthy volunteers in accordance with the Declaration of Helsinki protocol.

Note that full information on the approval of the study protocol must also be provided in the manuscript.

Clinical data

Policy information about [clinical studies](#)

All manuscripts should comply with the ICMJE [guidelines for publication of clinical research](#) and a completed [CONSORT checklist](#) must be included with all submissions.

Clinical trial registration

NCT02269592

Study protocol

IRB 14-174 (<https://clinicaltrials.gov/ct2/show/NCT02269592?term=irene+ghobrial&rank=2>), 07-150 (internal DFCI tissue banking study)

Data collection

Tissue banking began in 2007 and 2014 for DFCI protocols 07-150 and 14-174, respectively. Both protocols had overall study oversight dedicated by select staff at the Dana-Farber Cancer Institute, including coordination with outside sites, database maintenance, consents, and questionnaire and sample collection. The Partners-hosted and encrypted data integration platform RedCap was utilized for maintaining study data. 14-174 patients who signed consent were given a link to REDCap where they had access to personalized, password-protected forms, including: Demographic Information Form, Main Consent Form, Patient Information Sheet, Authorization for Release of Protected Health Information, Intake Survey, and Baseline Questionnaire. Similarly, all patient-derived materials were tracked using caTissue for centralized specimen management, including detailed tracking of specimens and derivative material, storage location, retrieval, and usage information. A specimen ID number was used to uniquely identify biological samples during all aspects of experimentation so that the resulting data can be linked to specimen and clinical data. Researchers and staff who are not authorized to see this information were blocked from viewing following HIPAA guidelines using role-based access controls.

Outcomes

No outcome was assessed. The study was designed to gain information about early changes in disease development and not connected to any treatment strategies. For MM patients, only untreated samples were used.

Flow Cytometry

Plots

Confirm that:

- The axis labels state the marker and fluorochrome used (e.g. CD4-FITC).
- The axis scales are clearly visible. Include numbers along axes only for bottom left plot of group (a 'group' is an analysis of identical markers).
- All plots are contour plots with outliers or pseudocolor plots.
- A numerical value for number of cells or percentage (with statistics) is provided.

Methodology

Sample preparation

Sample preparation was performed accordingly to the guidelines for two-step protocol: intracellular (cytoplasmic) proteins from thermofisher (BestProtocols: Staining Intracellular Antigens for Flow Cytometry), <https://www.thermofisher.com/us/en/home/references/protocols/cell-and-tissue-analysis/protocols/staining-intracellular-antigens-flow-cytometry.html#cytoplasmic>

Instrument

BD Canto II, BD Fortessa, BD Aria

Software

Premium Cyto bank, FlowJo

Cell population abundance

n/a

Gating strategy

Acquired events were gated accordingly their position on FSC/SSC plot, dead cells (positive for live/dead Aqua staining) were excluded from the analysis. An example of gating strategy is shown in Supplemental fig. 7. For cell sorting experiments, doublets were excluded based on the position on SSC-H/SSC-W and FSC-H/FSC-W axes

Tick this box to confirm that a figure exemplifying the gating strategy is provided in the Supplementary Information.